Article

Developmental Cell

S-Palmitoylation Sorts Membrane Cargo for Anterograde Transport in the Golgi

Graphical Abstract

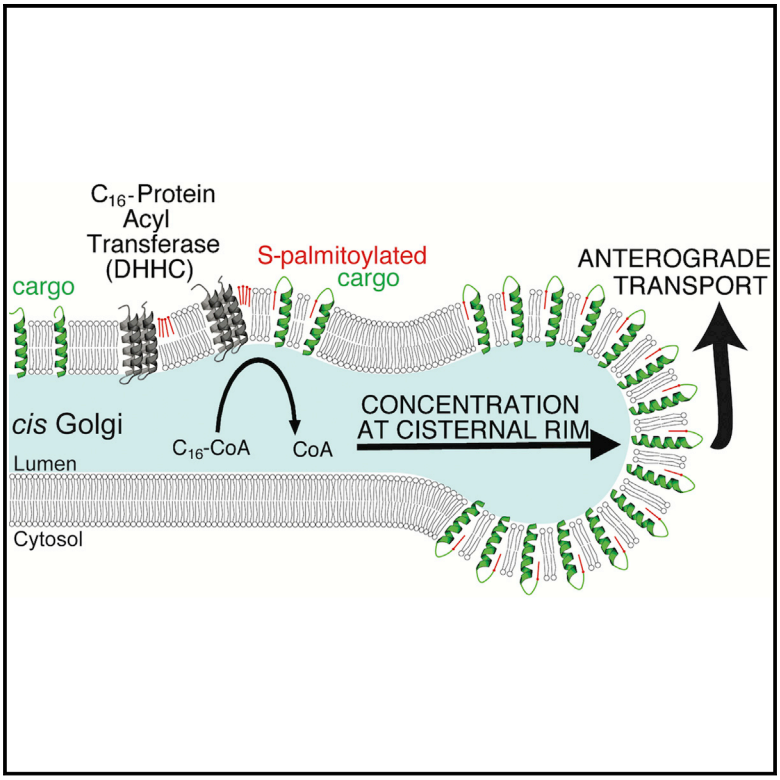

Highlights

- DHHC S-palmitoyltransferases are enriched in the *cis*-Golgi
- S-palmitoylation induces concentration of membrane cargo at the cisternal rim
- The rate of anterograde transport across the Golgi is controlled by S-palmitoylation

Authors

Andreas M. Ernst, Saad A. Syed, Omar Zaki, ..., Derek Toomre, Frederic Pincet, James E. Rothman

Correspondence

andreas.ernst@yale.edu (A.M.E.), james.rothman@yale.edu (J.E.R.)

In Brief

Examples exist of secretory pathway receptor-mediated protein sorting for retrograde cargo, but not for anterograde. Ernst et al. uncover an anterograde cargo sorting mechanism: S-palmitoylation at the Golgi acts as a biophysical switch that induces "self-sorting" of membrane cargo to the cisternal rim, enabling its efficient transport through the Golgi.

Ernst et al., 2018, Developmental Cell *47*, 479–493
November 19, 2018 © 2018 Elsevier Inc.
https://doi.org/10.1016/j.devcel.2018.10.024

CellPress

Developmental Cell
Article

S-Palmitoylation Sorts Membrane Cargo for Anterograde Transport in the Golgi

Andreas M. Ernst,[1,3,*] Saad A. Syed,[1] Omar Zaki,[1] Francesca Bottanelli,[1] Hong Zheng,[1] Moritz Hacke,[1] Zhiqun Xi,[1] Felix Rivera-Molina,[1] Morven Graham,[1] Aleksander A. Rebane,[1] Patrik Björkholm,[1] David Baddeley,[1] Derek Toomre,[1] Frederic Pincet,[1,2] and James E. Rothman[1,*]

[1]Department of Cell Biology, Yale School of Medicine, New Haven, CT 06520, USA

[2]Laboratoire de Physique Statistique, Ecole Normale Supérieure, PSL Research University, Université Paris Diderot Sorbonne Paris Cité, Sorbonne Universités UPMC Univ, CNRS, Paris, France

[3]Lead Contact

*Correspondence: andreas.ernst@yale.edu (A.M.E.), james.rothman@yale.edu (J.E.R.)

https://doi.org/10.1016/j.devcel.2018.10.024

SUMMARY

While retrograde cargo selection in the Golgi is known to depend on specific signals, it is unknown whether anterograde cargo is sorted, and anterograde signals have not been identified. We suggest here that S-palmitoylation of anterograde cargo at the Golgi membrane interface is an anterograde signal and that it results in concentration in curved regions at the Golgi rims by simple physical chemistry. The rate of transport across the Golgi of two S-palmitoylated membrane proteins is controlled by S-palmitoylation. The bulk of S-palmitoylated proteins in the Golgi behave analogously, as revealed by click chemistry-based fluorescence and electron microscopy. These palmitoylated cargos concentrate in the most highly curved regions of the Golgi membranes, including the fenestrated perimeters of cisternae and associated vesicles. A palmitoylated transmembrane domain behaves similarly in model systems.

INTRODUCTION

What are the basic principles of cargo selection for anterograde transport in the Golgi stack? Thirty years ago, we first reported that palmitoyl (C16)-coenzyme A (coA) stimulated intra-Golgi transport in a cell-free extract (Glick and Rothman, 1987). Removing palmitoyl-CoA from the extract revealed a strong requirement for acyl-CoA, which was met only by palmitoyl-CoA and not C14 or C18 acyl-CoAs. Transport was inhibited by adding a non-hydrolyzable analog of palmitoyl-CoA, confirming that acyl chain transfer to an acceptor was required. Remarkably, the assembly of COPI-coated vesicles from the Golgi cisternal rims, containing the cargo protein VSV G, was revealed to be strongly dependent on this palmitoylation event (Pfanner et al., 1989). The molecular basis of this striking and fundamental finding has remained obscure since then.

Now, as a result of important progress in understanding the enzymes that mediate palmitoylation (Fukata et al., 2004; Lobo et al., 2002; Roth et al., 2002; Politis et al., 2005) and advances allowing sites of palmitoylation to be visualized by light microscopy (Kolb et al., 2001), as well as broad advances in molecular cell biology, this investigation is now in a position to be reopened. A large variety of transmembrane and soluble proteins are modified with palmitate by its attachment onto cysteine residues of proteins via a thioester linkage, which strikingly can alter the biophysical properties of the acylated proteins (Smotrys and Linder, 2004). In most cases, these sites of acylation are retained, while in other cases, particularly for soluble proteins involved in signaling cascades, a highly dynamic turnover is observed (Fukata and Fukata, 2010; Linder and Deschenes, 2007; Demers et al., 2014; El-Husseini et al., 2002; Salaun et al., 2010). Furthermore, S-palmitoylation was shown to induce wide ranging regulatory effects on proteins, including membrane-targeting, protein-protein interactions, protein folding and stability, sorting of soluble palmitoylated proteins to the plasma membrane (Salaun et al., 2010; Linder and Deschenes, 2007), and, recently, modulation of membrane protein spontaneous curvature (Chlanda et al., 2017). Currently, proteomic analysis has identified more than 500 proteins as S-palmitoylated, which includes both integral and peripheral membrane proteins (Blanc et al., 2015). Given the ubiquity of S-palmitoylation and its involvement in key physiological processes, it is no surprise that palmitoylation has been linked to a number of human diseases (Greaves and Chamberlain, 2011).

In mammals, S-palmitoylation is catalyzed by a family of 23 acyltransferase enzymes (Fukata et al., 2004; Lobo et al., 2002; Roth et al., 2002). These enzymes share a conserved membrane topology with 4–6 transmembrane domains, as well as a prominent DHHC tetrapeptide positioned in a cysteine-rich domain (CRD) that is crucial for acylation activity (Politis et al., 2005). The DHHC-CRD domain resides on a cytosolic loop, thereby allowing it to access substrates close to the membrane. Palmitoylation by DHHC enzymes is thought to occur via a two-step mechanism in which the DHHC enzymes first form an acyl-enzyme intermediate on cysteine residues (autoacylation) and then subsequently transfer the palmitate to a cysteine residue on the target protein (Jennings and Linder, 2012; Mitchell et al., 2010). Recently, the structure of DHHCs 15 and 20 was solved in a lipidic cubic phase, suggesting the orientation of the active site close to the membrane (Rana et al., 2018). Early biochemical and localization studies have concluded that the

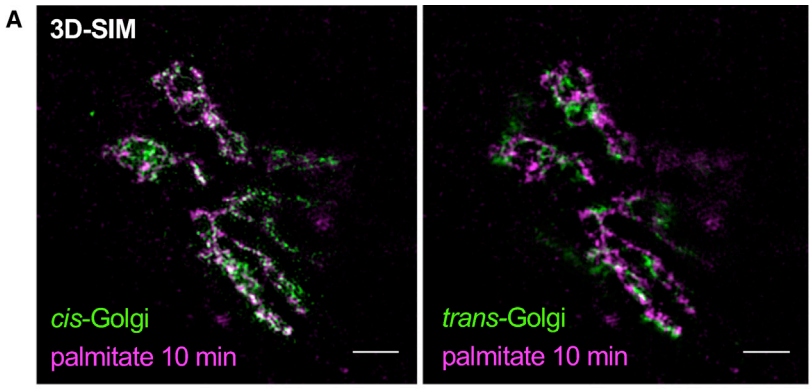

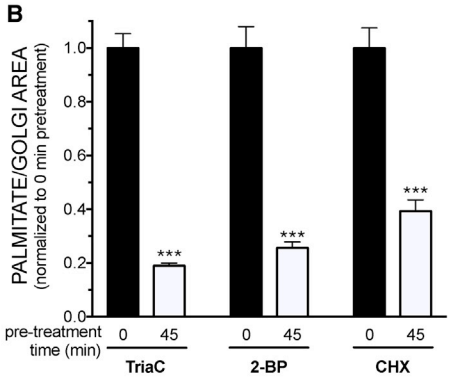

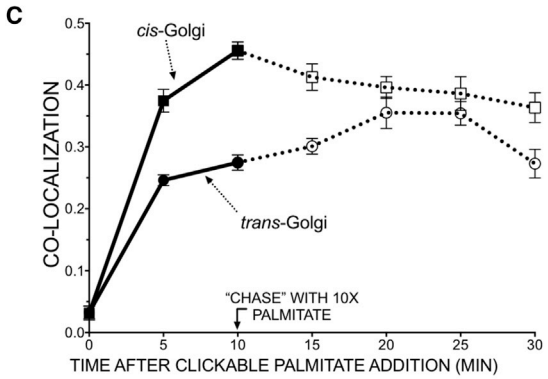

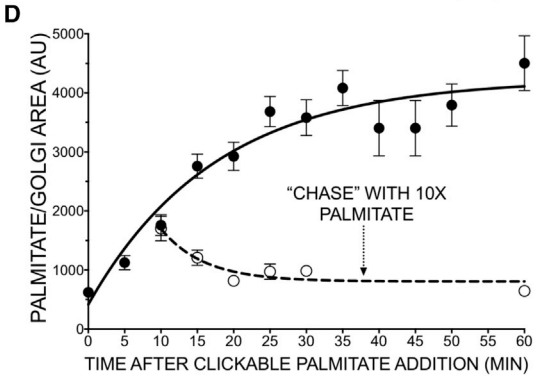

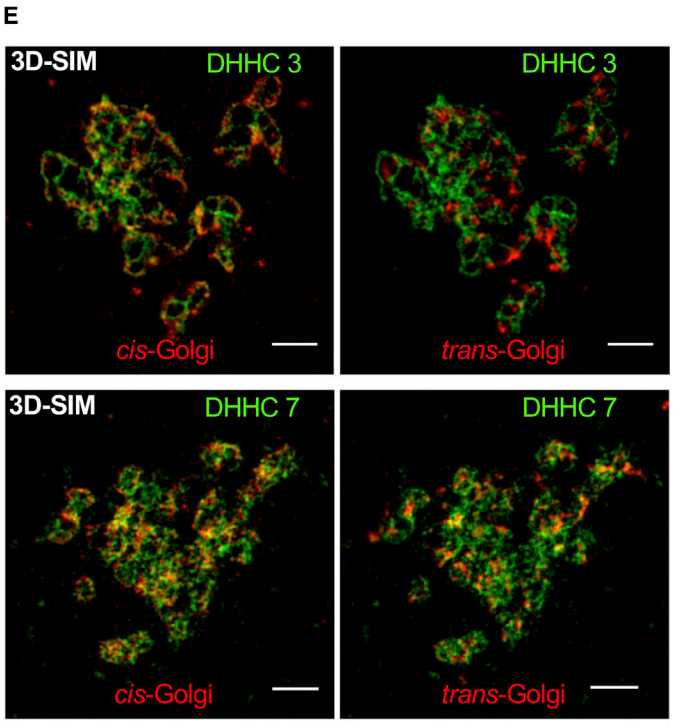

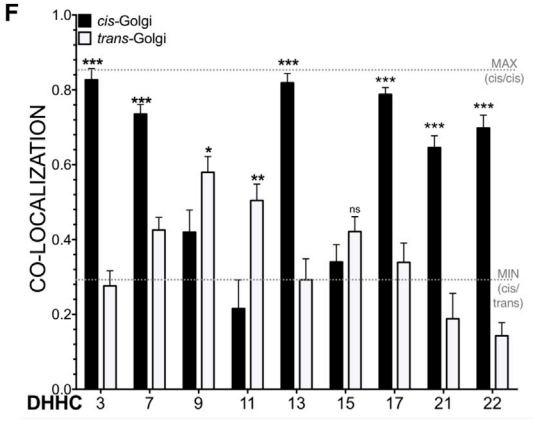

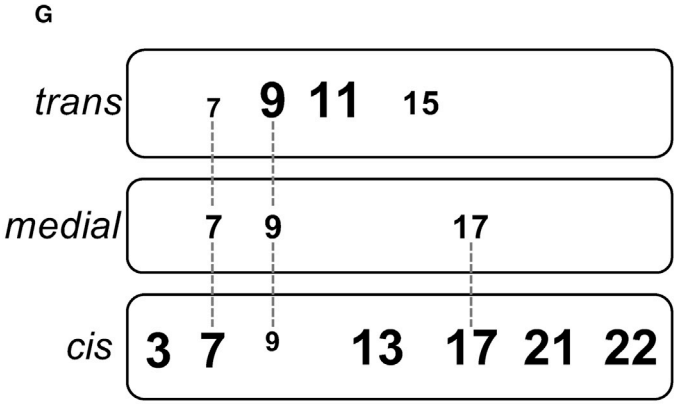

(legend on next page)

majority of the DHHC enzymes reside on the endoplasmic reticulum (ER) and the Golgi apparatus (Ohno et al., 2006).

In the present study, we revisit the requirement for palmitoyl-CoA on the sorting and trafficking of protein cargo within the Golgi. We mapped the subcellular localization of the 23 DHHC isoforms and discovered that the majority of Golgi-localized DHHCs are concentrated in the *cis*-Golgi. By employing a metabolic labeling strategy paired with click chemistry and super-resolution fluorescence and electron microscopy, we confirmed that the bulk of palmitate was incorporated into anterograde cargo into the *cis*-Golgi. Unexpectedly, we discovered that palmitoylation in the *cis*-Golgi accelerates the transport of these proteins through the Golgi. Strikingly, the palmitoylated proteins are concentrated in the highly curved rims of the *cis*-Golgi, which we suggest may explain the observed acceleration in rate.

RESULTS

Anterograde Transported Cargo Is S-Palmitoylated in the *cis*-Golgi, and Golgi-Localized DHHCs Are Concentrated in the *cis*

In order to identify the main site of bulk S-acylation in HeLa cells, a metabolic labeling strategy was combined with a click chemistry-based approach (Kolb et al., 2001). HeLa cells were labeled with different molecular species of fatty acid analogs, fixed, and subjected to a copper-dependent azide-alkyne cycloaddition (CuAAC) to azide-Alexa 647. Only the C16 and C18 probes efficiently labeled the Golgi, but not the C14 analog, while lipid-droplet-like structures were observed in each case (Figures 1A and S1A). Importantly, labeling of the Golgi with the C16 probe required activation with CoA (sensitive to Triacsin C [TriaC], inhibitor of the long chain fatty acid CoA synthetase; Omura et al., 1986), catalysis by DHHC palmitoyltransferases (sensitive to 2-bromopalmitate [2-BP], inhibitor of DHHCs; Coleman et al., 1992), and the presence of biosynthetic cargo at the Golgi (sensitive to cycloheximide [CHX]-induced purge of the Golgi; Taylor et al., 1984; Todorow et al., 2000), altogether supporting that the majority of signal observed stemmed from S-palmitoylated proteins (Figures 1B and S1B–S1D). Furthermore, the use of C16 and C18 probes coincided with the appearance of distinct protein bands after SDS-PAGE and in-gel fluorescence, which, as expected of S-palmitoylated proteins, were hydroxylamine sensitive (Figure S1E), cleaving S-linked acyl bonds rather than O-linked acyl bonds (Magee et al., 1984). We next quantified the co-localization of the (C16) palmitate probe at different times of labeling from confocal z stacks with regard to endogenous *cis*- and *trans*-Golgi markers, the ER, and lipid droplets (Figure S1F). The majority of the observed signal over the course of the pulse originated from the Golgi and lipid droplets. 3D structured illumination super-resolution microscopy (SIM) revealed that within the Golgi, the main site of incorporation was in the *cis*-compartment (Figures 1A and 1C). Within the next 10 min of a "chase" experiment, in which an excess of natural palmitic acid was added to largely replace the analog from that time onward, co-localization with the *cis*-Golgi declined while increasing in the *trans*-Golgi (with no appearance of the probe in the ER; Figures 1C and S1G). This would be expected if the bulk of labeled proteins was anterograde-directed cargo. Consistent with this finding, the bulk of the protein at the Golgi exited within 20 min, as revealed by quantifying several hundreds of cells in a "chase" experiment (Figures 1D and S1H).

Palmitoylation of Cysteine residues in membrane proteins occurs at juxta-membrane positions, with more than 500 proteins previously identified via proteomic analyses (Blanc et al., 2015). Several DHHC palmitoyltransferases are localized within the Golgi (Ohno et al., 2006). These enzymes generally accept C16 (palmitate) and to a lower extent C18 (stearate), but not shorter (C14, myristate) fatty acids as coA-activated substrates (Politis et al., 2005; Jennings and Linder, 2012; Mitchell et al., 2010). S-palmitoylation in the *cis*- prior to the *trans*-Golgi suggested the presence of distinct DHHCs in the *cis*-Golgi. In order to identify DHHC isoform candidates that exclusively localize to the Golgi, the subcellular localization of a mouse ortholog library of all 23 DHHCs was mapped (Fukata et al., 2004). Indeed, 17 of the 23 DHHCs exhibited a partial Golgi localization, with 11 predominantly localizing to the Golgi (Figures S2A–S2C). The corresponding human orthologs were cloned as aminoterminal fusion proteins to the SNAP-tag protein, and the intra-Golgi localization of the human DHHC candidates was then probed with endogenous *cis*- and *trans*-Golgi markers using confocal microscopy (Figures 1F and S2D). While the human DHHC 16 and 18 localized to the ER and PM, respectively, the remaining 9 candidates

Figure 1. Anterograde Transported Cargo Is S-Palmitoylated in the *cis*-Golgi, and Golgi-Localized DHHCs Are Concentrated in the *cis*

(A) HeLa cells were metabolically labeled with 50 μM alkyne-palmitate for 10 min, fixed, permeabilized, clicked to azide-AF647, immunostained for endogenous Golgi markers (*cis*-Golgi: GPP130, *trans*-Golgi: p230), and subjected to structured illumination super-resolution microscopy (3D-SIM, max. intensity Z-projections; scale bars: 2 μm).

(B) Labeling of the Golgi with alkyne-palmitate requires CoA-activation, DHHC enzyme function, and the presence of biosynthetic cargo. Pretreatment of cells with Triacsin C (TriaC, 100 μM, inhibitor of the long chain fatty acyl-CoA synthetase), 2-bromopalmitate (2-BP, 100 μM, competitive DHHC inhibitor), or CHX (100 μg/mL, inhibitor of protein biosynthesis) for 45 min prior to a 10-min pulse of alkyne-palmitate prevents Golgi labeling. The average integrated intensity of alkyne-palmitate signal at the Golgi in the presence of inhibitors was quantified and compared to mock-treated controls ($n > 60$ cells/time point and condition, mean and SEM, two-tailed unpaired t tests [***: $p < 0.001$]).

(C) 3D-SIM of alkyne-palmitate with *cis*- and *trans*-Golgi markers for a 5- or 10-min pulse (50 μM), followed by a chase with natural palmitate at 10× molar excess after 10 min. Co-localization (Pearson's R) was determined and subjected to two-tailed, unpaired t tests ($n > 10$ cells/time point, mean and SEM).

(D) HeLa cells were constantly labeled with 50 μM alkyne-palmitate or pulsed for 10 min followed by a chase with natural palmitate at 10× molar excess (500 μM). After click chemistry, the integrated fluorescence intensity of the Golgi area was quantified ($n > 20$ cells/time point and condition, mean and SEM).

(E) Co-localization analysis of human DHHC 3 and 7 (3D-SIM). SNAP-DHHC isoforms were transfected for 24 hr. After fixation, endogenous Golgi markers were immunolabeled (*cis*-Golgi: GPP130, *trans*-Golgi: p230), and SIM images of the Golgi area were obtained (max. intensity Z-projections are given, scale bars: 2 μm).

(F) Localization of human DHHC candidates within the Golgi. SNAP-DHHC fusions of 9 Golgi candidates were scored for co-localization as described in (E), and subjected to two-tailed, unpaired t tests (ns: not significant; *: $p < 0.05$; **: $p < 0.01$; ***: $p < 0.001$; $n > 20$ cells/time point, mean and SEM).

(G) Schematic of the localization of human DHHC palmitoyltransferases within the Golgi.

See also Figure S1.

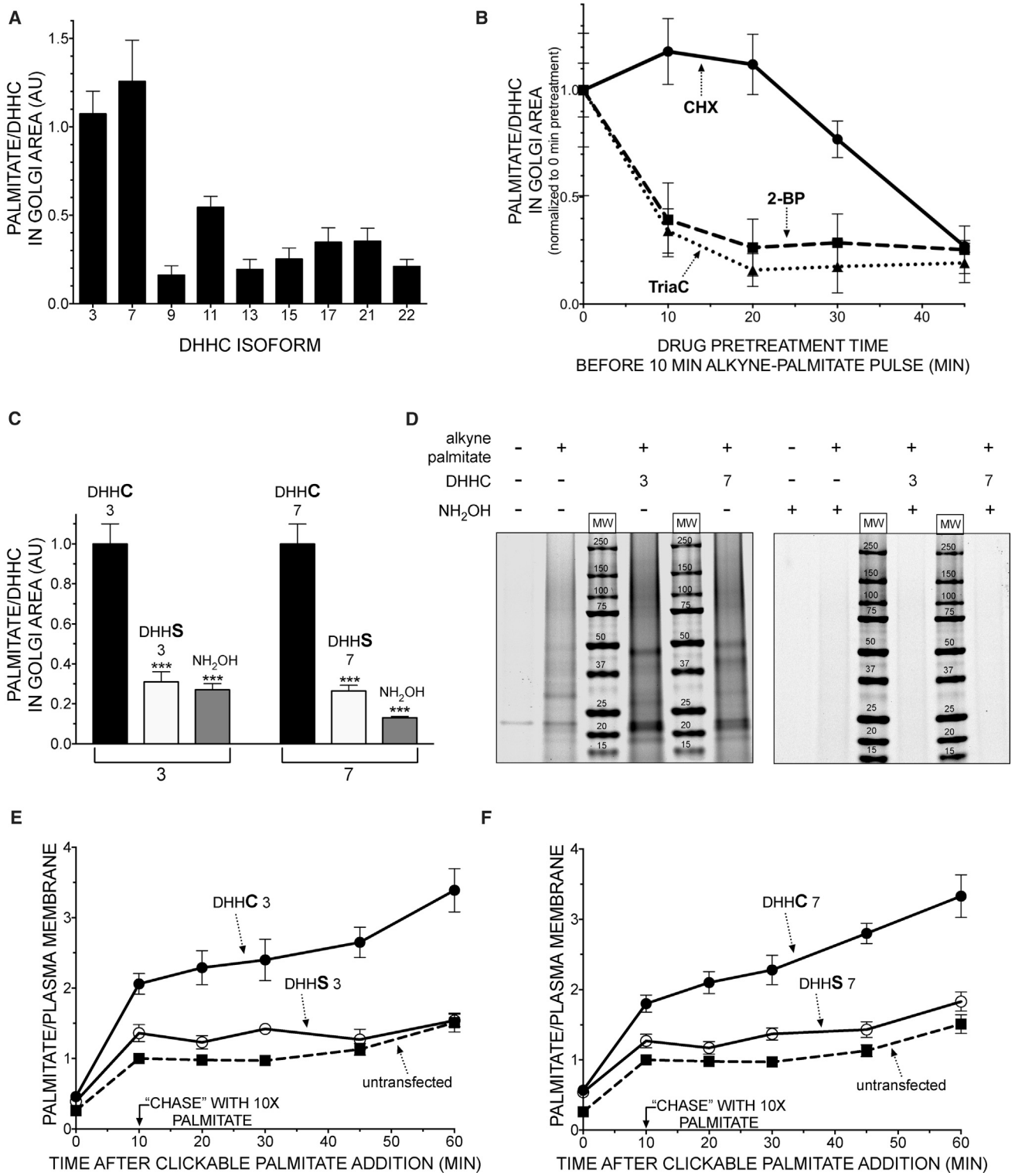

Figure 2. DHHCs 3 and 7 Account for the Majority of S-Palmitoylated Cargo Proteins at the Golgi and Catalyze Their Transport to the Plasma Membrane

(A) Human SNAP-tagged DHHC candidates were transiently transfected into HeLa cells and metabolically labeled with azide-palmitate for 20 min. The ratio of the integrated intensity of palmitate and the respective DHHC was quantified (n > 10, mean and SEM).

(B) HeLa cells overexpressing SNAP-DHHC3 were pretreated with Triacsin C (TriaC, 100 μM), 2-bromopalmitate (2-BP, 100 μM), or cycloheximide (CHX, 100 μg/mL) prior to a 10-min pulse with alkyne-palmitate. Confocal z stacks were obtained, and the ratio of palmitate to DHHC fluorescence was quantified as in (A) (n > 30 cells per time point and condition, mean and SEM).

(legend continued on next page)

exhibited an asymmetrical distribution across the *cis*-to-*trans* Golgi axis: DHHCs 3, 7, 13, 17, 21, and 22 specifically localized to the *cis*. zDHHCs 9, 11, and 15 localized partially to the *trans*-Golgi, and to differing extents, to post-Golgi structures (Figures 1G and S2D).

DHHCs 3 and 7 Account for the Majority of S-Palmitoylated Cargo Proteins at the Golgi and Catalyze Transport of Bulk S-Palmitoylated Anterograde Cargo to the Plasma Membrane

To determine which Golgi-localized S-palmitoyltransferases contribute to the observed incorporation of palmitate analog into anterograde cargo in the *cis*-Golgi (Figure 1C), each Golgi candidate (human) DHHC enzyme was overexpressed (Figures 2A and S2E). DHHC3 and DHHC7 dramatically increased both the rate of incorporation as well as the rate of Golgi exit when chased with natural palmitate (Figures S3A and S3B). Analogous to untransfected cells, DHHC-catalyzed S-palmitoylation at the Golgi required activation with CoA, DHHC enzyme function, and the presence of biosynthetic cargo (Figures 2B and S1B–S1D). Furthermore, the increased incorporation of palmitate in the Golgi area resulted from acyl transfer since enzymatically inactive versions of DHHC3 and DHHC7 (DHHS) did not increase the incorporation (Figures 2C, S3C, and S3D). As expected, the palmitate analog incorporated by both DHHC3 and DHHC7 was released from fixed, permeabilized cells upon exposure to hydroxylamine (Figures 2C and S1B).

Consistent with the initial concentration of basal alkyne-palmitate into the *cis*-Golgi (Figures 1A and 1C), DHHC3 and DHHC7 are localized to *cis*- but not *trans*-Golgi regions when co-localized with endogenous markers using 3D-SIM (Figures 1E and S3E). DHHC7 was recently mapped to the *trans*-Golgi, but by employing overexpressed Golgi markers (Du et al., 2017). In fact, we noticed that strong DHHC overexpression results in the disappearance of endogenous Golgi markers (Figure S3F) and conclude that the localization of these DHHCs within the stack can only be accurately mapped in the presence of these endogenous markers (at low DHHC expression levels). The closely related DHHCs 3 and 7 are ubiquitously expressed (Ohno et al., 2006), and various studies revealed that overexpression of the corresponding mouse orthologs efficiently catalyzed S-palmitoylation of a broad variety of substrates (Gottlieb et al., 2015; Greaves et al., 2017). DHHC3 and DHHC7 protein substrates consist of numerous distinct proteins visible in SDS-PAGE that are sensitive to hydroxylamine cleavage (Figure 2D).

As the rapid Golgi exit of S-palmitoylated proteins (with lack of rising palmitate levels in the ER) implied that the majority of DHHC substrates are anterograde cargo, putatively plasma membrane residents, bioinformatical predictions on compartment-specific datasets were performed (ER, Golgi, PM). We compared (1) the total fraction of proteins containing high-confidence S-palmitoylation sites, (2) the average number of predicted sites per protein, and (3) the fraction of proteins containing signal sequences, cytoplasmic Cys residues, and high-confidence S-palmitoylation sites (Figures S3G and S3H), supporting that indeed anterograde cargo are a major class of DHHC substrates, as all values peak in the PM dataset.

We therefore metabolically labeled cells expressing either DHHC3, 7, or their enzymatically inactive variants (DHHS) with alkyne-palmitate for 10 min, chased the probe for different times, and after fixation and permeabilization, performed total internal reflection fluorescence (TIRF) microscopy. Strikingly, overexpressing either DHHC3 or DHHC7 (Figures 2E, 2F, S4A, and S4B) markedly accelerated the rate and extent of appearance of S-palmitoylated proteins at the cell surface (3-fold after 60 min). Furthermore, this acceleration required active DHHC forms of the enzymes, with no acceleration observed with DHHS point mutants. To confirm transit of the anterograde palmitoylated cargo, a strategy was employed that would allow for transmission electron microscopy of palmitoylated proteins. HeLa cells were stably transfected with SNAP-DHHC3 to catalyze the incorporation of alkyne-palmitate into the Golgi (Figure S4C). Our previous approach was adapted by employing azide-biotin as a ligand for alkyne-palmitate, which was then detected using a fluorogold-labeled (containing 1.4 nm nanogold and Alexa488) Streptavidin, allowing the use of light and electron microscopy (Figure S4D). We again performed a time-course experiment to monitor the distribution of the probe within intracellular membranes over time, and its enrichment was quantified in the Golgi. In agreement with the partitioning of alkyne-palmitate observed through the Golgi on the light level (Figures 1 and 2), an extensive labeling of Golgi membranes after 30 min of pulse was confirmed (Figure S4E). After 60 min, a marked labeling of the plasma membrane concurrent with a reduction of membrane labeling within the Golgi was observed (Figures S4E and S4F).

Palmitoylation of Membrane Proteins Accelerates Their Rate of Intra-Golgi Protein Transport

The marked increase in the amount of S-palmitoylated protein detected at the plasma membrane upon overexpression of DHHC3 or 7 (in the *cis*-Golgi) prompted the hypothesis that palmitoylation accelerates trafficking of anterograde cargo at the level of the Golgi. There is some precedent as palmitoylation at the Golgi had been established as an important step in the vectorial transport of multiple *soluble* proteins, e.g., H-Ras, CSP, and SNAP25 (Gonzalo and Linder, 1998; Greaves et al.,

(C) Cells transfected with DHHC isoforms 3 and 7 or their enzymatically inactive (DHHS) variants were labeled with alkyne-palmitate for 20 min. To estimate the fraction of thioester-bound palmitate in the Golgi area, the samples were incubated with 1.5 M neutral hydroxylamine for 2 hr followed by an extensive washout. The ratio of palmitate and DHHC fluorescence was quantified, normalized to the respective wt construct, and subjected to two-tailed unpaired t tests (***: $p < 0.001$, $n > 50$ cells per condition, mean and SEM).

(D) Overexpressed DHHCs 3 and 7 catalyze S-palmitoylation of numerous protein substrates. Cells expressing SNAP-DHHC3, 7, or mock-transfected cells were labeled for 20 min with alkyne-palmitate, clicked to azide-AF647, and subjected to in-gel fluorescence analysis.

(E and F) Cells were transfected with DHHC isoforms 3 (E), 7 (F), or their inactive (DHHS) variants, metabolically labeled with alkyne-palmitate for 10 min and subjected to a chase with natural palmitate at 10× molar excess for the indicated time. After fixation, permeabilization, and labeling, the samples were subjected to TIRF microscopy ($n > 20$ cells per construct, time point, and condition, mean and SEM).

See also Figures S2–S4.

2008; Apolloni et al., 2000). For such soluble proteins, palmitoylation acts as a post-ER membrane-targeting signal, restricting peripheral protein function to the Golgi and PM, while enabling their release via thioesterases. Further, a plethora of integral membrane proteins has been identified as being S-palmitoylated, including most viral spike proteins, plasma membrane channels, and receptors (Schmidt and Schlesinger, 1979; Chien et al., 1996; Charollais and Van Der Goot, 2009). Would palmitoylation of individual anterograde (integral) membrane protein cargo impact their trafficking, as we observed for the bulk of palmitoylated proteins?

To investigate this in more detail, we compared the rate of anterograde transport of two well-characterized model palmitoylated cargo proteins (VSV G protein and transferrin receptor) compared to non-palmitoylated mutants in which the attachment site cysteines were mutated to alanines (VSVG-C490A, TfR-C62AC67A). S-palmitoylation for both model proteins depended on the presence of Cys and their release from the ER (Figures S5A and S5H). For VSV G, a wave of anterograde cargo can be generated by employing a temperature-sensitive mutant (tsO45, Bergmann, 1989) that under the non-permissive temperature (40.5°C) is blocked in the ER and can be released at 32°C. Employing a surface biotinylation strategy, we observed a marked difference in the amount detected on the cell surface 30 min post release from the ER: *wt* VSV G exhibited 50% increased PM levels, while similar levels of Cys→Ala VSVG were only observed after at 60 min (Figure 3A, upper left panel; Figure S5B).

Where did this acceleration occur? Over 30 years ago, Rose and colleagues had compared the rate of acquisition of EndoH resistance carbohydrates between *wt* and the same Cys→Ala mutant VSV G protein and did not observe any significant differences in these rates (Rose et al., 1984). We revisited these experiments, and indeed an identical rate of entry of *wt* and variant G into the Golgi was observed (Figure 3A, upper right panel; Figure S5C). EndoH-resistance is achieved upon arrival of the cargo in the *cis*-to-*medial* Golgi, where the concentrations of alpha-Mannosidases I/II peak, hence monitoring the rate of transport from the ER to the Golgi, but not beyond this point. We therefore speculated that any contribution of S-palmitoylation to ER→PM trafficking was not at the ER→Golgi but either within the Golgi or Golgi/TGN→PM.

When performing surface biotinylation experiments in conjunction with a 20°C block (to accumulate cargo in the TGN prior to its release), no differences were observed in surface arrival between the constructs (Figure 3A, lower left panel; Figure S5D), supporting a palmitoylation-dependent acceleration of G protein from the *cis*- to the *trans*-Golgi.

To test this possibility, the rate of acquisition of galactose was measured in the *trans*-Golgi by using the terminal galactose residue-specific lectin jacalin. While *wt* G rapidly became positive for galactose 10 min post release and was fully processed within the following 10 min, in which further extension of the N-glycans masks detection by jacalin, Cys→Ala G protein revealed a significantly delayed peak at 30 min and elevated levels even at 60 min (Figure 3A, lower right panel; Figure S5E). An accelerated arrival of *wt* G in the *trans*-Golgi was confirmed by confocal co-localization with endogenous Golgi markers (Figure S5F), excluding the possibility of an altered access to the glycosyltransferase within the *trans*-Golgi.

To assess whether these results are retained for a different palmitoylated membrane cargo independent of the temperature shift, we next employed a modified version of the transferrin receptor (TfR-FM4-HALO) containing FM domain repeats, leading to aggregation of the model cargo in the ER and allowing for a triggered release using a solubilizing drug (Bottanelli et al., 2016). Importantly, similar to VSV G, TfR has been established as palmitoylated protein at two juxtamembrane cysteine residues (C62 and C67; Alvarez et al., 1990). A Cys→Ala variant (C62A-C67A) was generated and live cell TIRF microscopy of single cells transfected with either construct was performed. In agreement with the impact of palmitoylation of G protein, surface arrival of palmitoylated TfR (Figure 3B, upper left panel; Figure S5I) was significantly delayed, with similar mutant surface levels observed only 90 min post release (Figures S5J and S5K). Again, this acceleration did not stem from different rates of ER→Golgi trafficking, which was concluded from time-course experiments in which *wt* or Cys→Ala TfR from the ER was released, and the extent of co-localization was monitored with a *cis*-Golgi marker (Figure 3B, upper right panel; Figure S5L). Employing a 20°C temperature block resulted in similar rates of surface arrival when measured by live cell TIRF microscopy (Figure 3B, lower left panel), while employing a 16°C block (*cis*-Golgi) resulted in an accelerated surface arrival for *wt* TfR (Figure S5M). In agreement with VSV G, these data strongly suggest an acceleration of intra-Golgi transport for palmitoylated TfR. The acquisition rate of galactose in the *trans*-Golgi was again monitored. Peaks for *wt* TfR were observed at 30 min, while the non-palmitoylated mutant exhibited a 20-min delay, peaking at 50 min post release (Figure 3B, lower right panel; Figure S5N).

In summary, for both model palmitoylated anterograde cargo proteins, the acceleration of transport only occurred within the Golgi, indicated by the observation that neither the kinetics of transport from ER→Golgi nor TGN→PM was affected by palmitoylation. Confirming this result, the rate of transit from ER→TGN was accelerated for both cargo proteins by palmitoylation, strongly supporting the finding that central regulation of anterograde traffic occurs by palmitoylation at the *cis*-Golgi.

Modulation of DHHC Levels and Their Activity Impacts Transport of Both Membrane and Secretory Proteins

Overexpression of DHHC3 and 7 had significantly catalyzed partitioning of S-palmitoylated proteins as a class to the plasma membrane (Figures 2E, 2F, and S4A). We therefore set out to test the effect of modulation of S-palmitoylation on the trafficking of two reporter proteins, VSV G and TfR, from the ER to the plasma membrane. The anterograde trafficking was examined in three conditions: (1) upon overexpression of DHHC3; (2) inhibition of global S-palmitoylation with 2-BP; and (3) inhibition of de-palmitoylation with palmostatin B (PB). We employed surface biotinylation experiments to monitor bulk arrival of VSV G at the plasma membrane. While in untreated cells a 2- to 3-fold increase in surface palmitoylated G was observed, no significant difference was observed in 2-BP-pretreated cells (Figures 4A, 4B, and S5G). Interestingly, either overexpression of DHHC3 or inhibition of de-palmitoylation with PB markedly accelerated surface arrival of *wt* and C490 variants. A corresponding acceleration in surface arrival was also detected for the TfR reporter: PM levels increased 3-fold after 60 min, whereas cells pretreated

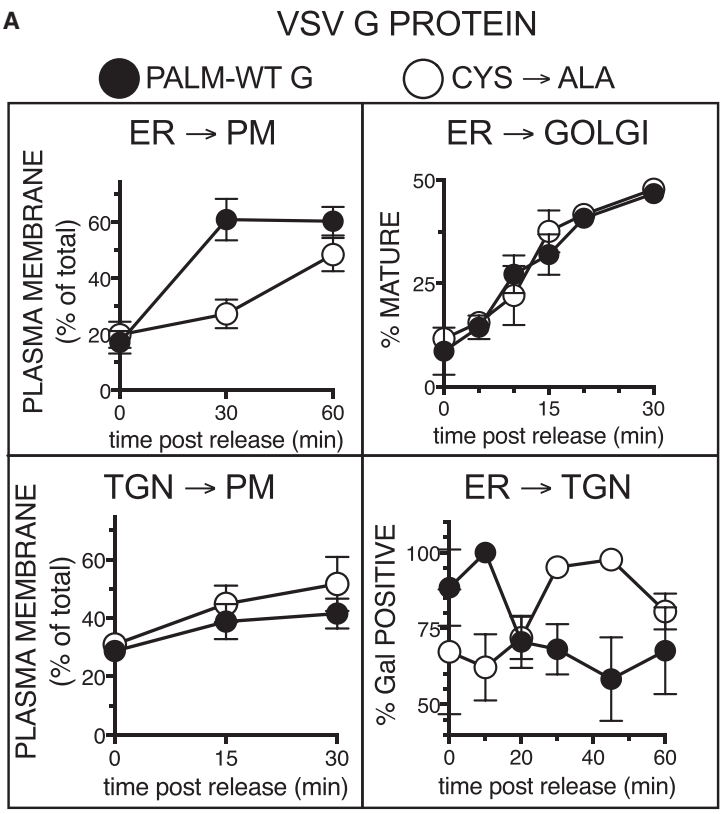

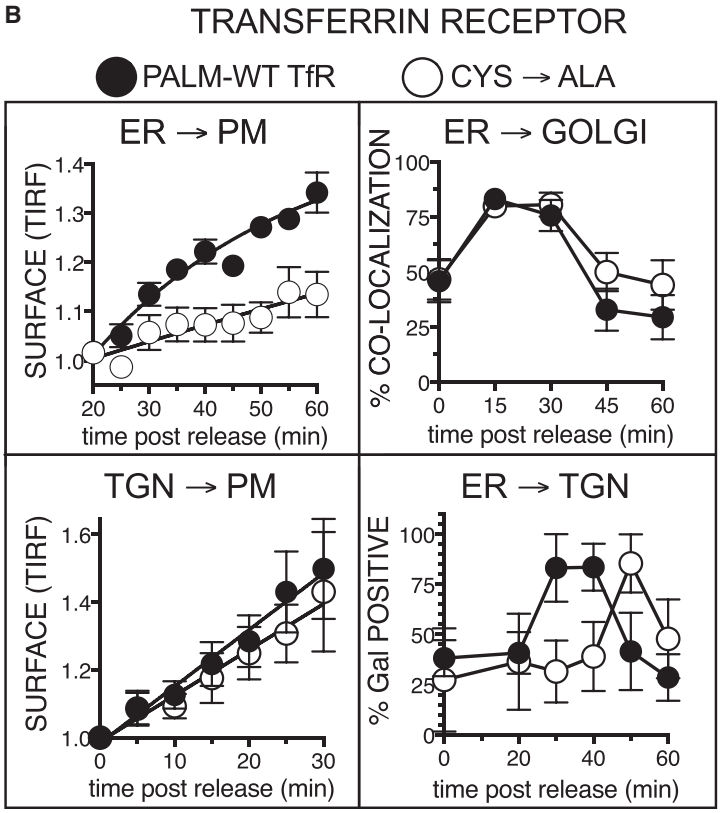

Figure 3. Palmitoylation of Membrane Proteins Accelerates Their Rate of Intra-Golgi Protein Transport

(A) HeLa cells transfected with wt VSVG-GFP or its non-palmitoylated variant VSV G-C490-GFP were shifted from non-permissive (40.5°C) to permissive temperature (32°C) to generate an anterograde wave of cargo. Upper left panel: surface arrival of S-palmitoylated VSV G is accelerated. Cells transfected with VSV G or C490A were released from the ER and subjected to surface biotinylation with sulfo-NHS-biotin at the indicated time point. A ratio of surface to total was quantified for n = 3 independent experiments (mean and SEM). Upper right panel: S-palmitoylation of VSV G does not impact the rate of entry into the Golgi. Constructs were released from the ER, and the rate of acquisition of EndoH-resistant N-glycans was monitored via western blot. Quantification of n = 4 independent experiments (mean and SEM). Lower left panel: surface arrival does not differ after release from the *trans*-Golgi/TGN. Cargo was arrested in the *trans*-Golgi via a 20°C block for 2 hr prior to releasing the temperature block for the indicated times. Quantification of n = 3 independent experiments (mean and SEM). Lower right panel: pull-down experiments employing the galactose-specific lectin jacalin. Quantification of n = 3 independent experiments, normalized to wt G peak at 10 min (mean and SEM).

(B) HeLa cells transfected with transferrin receptor (TfR-FM4-HALO) or its non-palmitoylated variant (TfR-C62AC67A-FM4-HALO) were released from the ER using a cell-permeable small molecule solubilizer (D/D) to generate an anterograde wave of cargo. Upper left panel: the rate of surface arrival was quantified employing live-cell TIRF imaging. The integrated intensity per cell over time from n = 4 independent experiments per construct and condition was quantified and normalized to initial fluorescence intensity (mean and SEM). Upper right panel: co-localization with a *cis* Golgi marker (HPL) after release from the ER for the indicated times. Quantification of n > 20 cells per time point and construct (mean and SEM). Lower left panel: surface arrival of TfR constructs does not differ when released from *trans*-Golgi/TGN. Live TIRF imaging of cells transfected with TfR constructs was performed after a 20°C block for 2 hr in the presence of D/D solubilizer. Quantification of n > 5 cells per construct (mean and SEM). Lower right panel: acquisition of galactose in the *trans*-Golgi is accelerated for palmitoylated TfR. Acquisition of galactose in the *trans*-Golgi was monitored as for VSV G in (A) by employing jacalin. Quantification of n = 3 independent experiments (mean and SEM).

See also Figure S5.

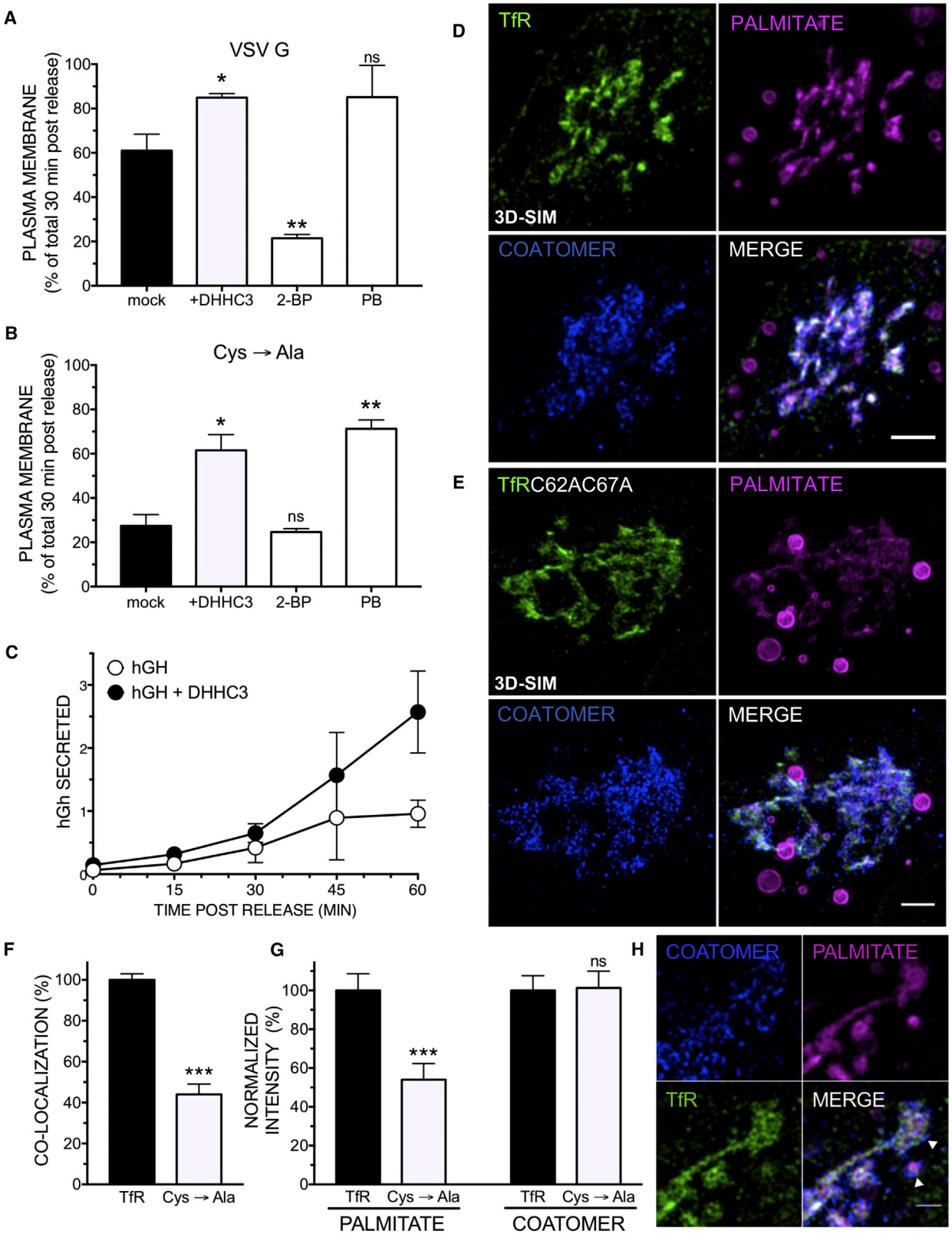

Figure 4. Modulation of DHHC Levels and Their Activity Impacts Transport of Both Membrane and Soluble Proteins

(A and B) Modulation of VSV G surface arrival by overexpression of SNAP-DHHC3, the competitive DHHC inhibitor 2-bromopalmitate (2-BP), or the de-palmitoylation inhibitor palmostatin B (PB). HeLa cells were transfected with VSV G (A) or C490A (B) for 24 hr and incubated at 40.5°C. If indicated, expression of

(legend continued on next page)

with 2-BP exhibited a marked reduction in TfR at the plasma membrane (Figures S5O and S5P).

The acceleration in transport observed for G and TfR model Cys→Ala variants upon overexpression of DHHC 3 (Figures 4B and S5O) prompted us to test whether overexpression of DHHC and the resultant increase in the rate of transport of S-palmitoylated proteins through the Golgi could globally impact secretion. We thus probed an FM-domain-containing model secretory protein, the human growth hormone (hGH-FM4-GFP), and monitored the fraction of hGH secreted in presence or absence of overexpressed DHHC3 (Figures 4C and S5Q). Strikingly, levels of hGH increased 3-fold in the medium of cells with a concomitant reduction of intracellular levels 60 min post release from the ER.

Palmitoylated Membrane Cargo Concentrates in Highly Curved Regions at the Cisternal Rims of the Golgi

Altogether, the data thus far supported that S-palmitoylation of membrane proteins results in higher rates of anterograde transport from the *cis*- to *trans*-Golgi. These results implied that S-palmitoylated proteins are sorted differentially upon entry into the Golgi, which prompted us to perform 3D-SIM of *wt* and Cys→Ala TfR constructs upon entry into the Golgi. Strikingly, *wt* and mutant TfR exhibited a marked differential distribution: *wt* appeared clustered, while mutant TfR appeared dispersed across *cis*-Golgi membranes (Figures 4D and 4E). Furthermore, labeling of the Golgi area with palmitate increased significantly in the presence of *wt* TfR, with the increase in staining stemming from areas that co-localized with the protein and that were juxtaposed by coatomer (Figures 4D–4H).

The differential distribution of TfR constructs in the Golgi prompted us to localize S-palmitoylated proteins as a class and at high resolution employing STED nanoscopy. Cells were pulsed with alkyne-palmitate and probed for a nanoscale co-localization with coatomer (marker of the highly curved cisternal rim) or a marker for the flat centers of *cis*-Golgi cisternae (GM130). Strikingly, coatomer-positive clusters representing putative COPI buds or vesicles at the Golgi were frequently observed that were enriched in palmitate (Figure 5A). We next set out to quantify the average proximity of COPI to S-palmitoylated proteins, finding that the majority (~93%) of COPI structures were positioned within 100 nm of S-palmitoylated proteins. On the other hand, GM130 appeared segregated from COPI with only ~44% of coatomer signal within 100 nm (dashed line) from the cisternal center (Figure 5B).

To obtain further clues as to the underlying mechanisms, we obtained double-tilt electron tomograms of cells pulsed with alkyne-palmitate and generated 3D models of the position of S-palmitoylated proteins with the underlying Golgi membranes (Figures S6A–S6E). First, we systematically quantified the local curvature encountered in the entire Golgi (Figure S6F) before and after a pulse of palmitate. Strikingly, the distribution drastically shifted toward the presence of highly curved membranes as palmitate was incorporated into the Golgi (Figure S6G). It was evident upon inspection that the gold-labeled palmitoylated proteins were concentrated in the highly curved tubulovesicular rims of the stack (Figures 5C and S6A–S6E). To quantify this effect, we measured the underlying local curvature at all positions within the tomogram exhibiting palmitate labeling and compared it to the local curvature distribution of Golgi membranes as a whole (Figures 5D and S6F). Strikingly, palmitoylated cargo exhibited a strong preference for membranes whose local radius of curvature was <50 nm, about the size of a COPI transport vesicle and the tubular-vesicular network encountered at the rim of Golgi cisternae (“non-compact region”; Ladinsky et al., 1999). These palmitoylated cargo could either be acylated within the curved regions or concentrate there after being palmitoylated elsewhere, depending on where the DHHC enzymes are localized. In fact, DHHCs are located separately from their palmitoylated products, co-localizing instead at the light level with markers of the stacked, flat regions of the Golgi cisternae (Figure S6H), suggesting that the palmitoylated cargo migrates from its site of synthesis in the stacked regions of the *cis* Golgi to concentrate at the tubule-vesicular rims.

Curvature Preference May Be an Intrinsic Property of Palmitoylated Anterograde Cargo

These results suggest that palmitoylated cargo—on the basis of the acyl chain—concentrate in highly curved Golgi rims and when they do so in large numbers actually increase the proportion of membrane in such curved regions, thereby putatively resulting in higher rates of overall anterograde transport. The simplest basis for these effects of the acyl chain would be physical-chemical. In other words, an increase in the intrinsic preference of the cargo membrane protein for curved membranes due to the physical chemistry of the fatty acid chain.

DHHC3 was induced in the stably transfected cells for 5 hr. Un-induced, VSV G-transfected parallel setups were incubated for 1 hr with 2-BP (100 μM) or PB (25 μM). VSVG was released from the ER for 30 min prior to biotinylation of surface-exposed proteins. Quantification of n = 3 independent experiments, mean and SEM. The results of two-tailed, unpaired t tests are given (ns: not significant; *: $p < 0.05$; **: $p < 0.01$).

(C) Overexpression of DHHC3 modulates the secretion of soluble cargo. The model protein hGh-FM4-GFP was transfected into dox-SNAP-DHHC3 cells. Expression was induced for 5 hr, prior to releasing hGh from the ER for the indicated times using D/D solubilizer. Cell contents were compared to hGh in the medium after chloroform-methanol precipitation (quantification of n = 3 independent experiments, mean and SEM). Upon entry into the Golgi, S-palmitoylated TfR segregates with palmitate into areas enriched with coatomer.

(D and E) 3D-SIM of TfR-FM4-SNAP (D) or TfRC62AC67A-FM4-SNAP (E) 15 min post release from the ER with a simultaneous metabolic labeling using alkyne-palmitate. After fixation, S-palmitoylated proteins were subjected to CuAAC to azide-AF647, and SNAP-tagged TfR constructs (AF488) and endogenous coatomer (CM1, AF568) were immunolabeled.

(F) Quantification of co-localization (Pearson’s R) of TfR constructs with palmitate in the *cis* Golgi (15 min post release from the ER; n = 30 cells/construct; SIM max. intensity Z-projections, normalized to *wt* TfR).

(G) Quantification of the ratio (integrated intensity) of palmitate and coatomer per TfR construct and for the Golgi area as in (F).

(H) Zoom-in of Golgi area indicating enlarged cisternal rims (15 min post release of TfR from the ER). White arrowheads: putative carriers positive for TfR, palmitate, and encompassed with coatomer (lower arrow), TfR-enriched rim area (upper arrow). Scale bar: 1 μm.

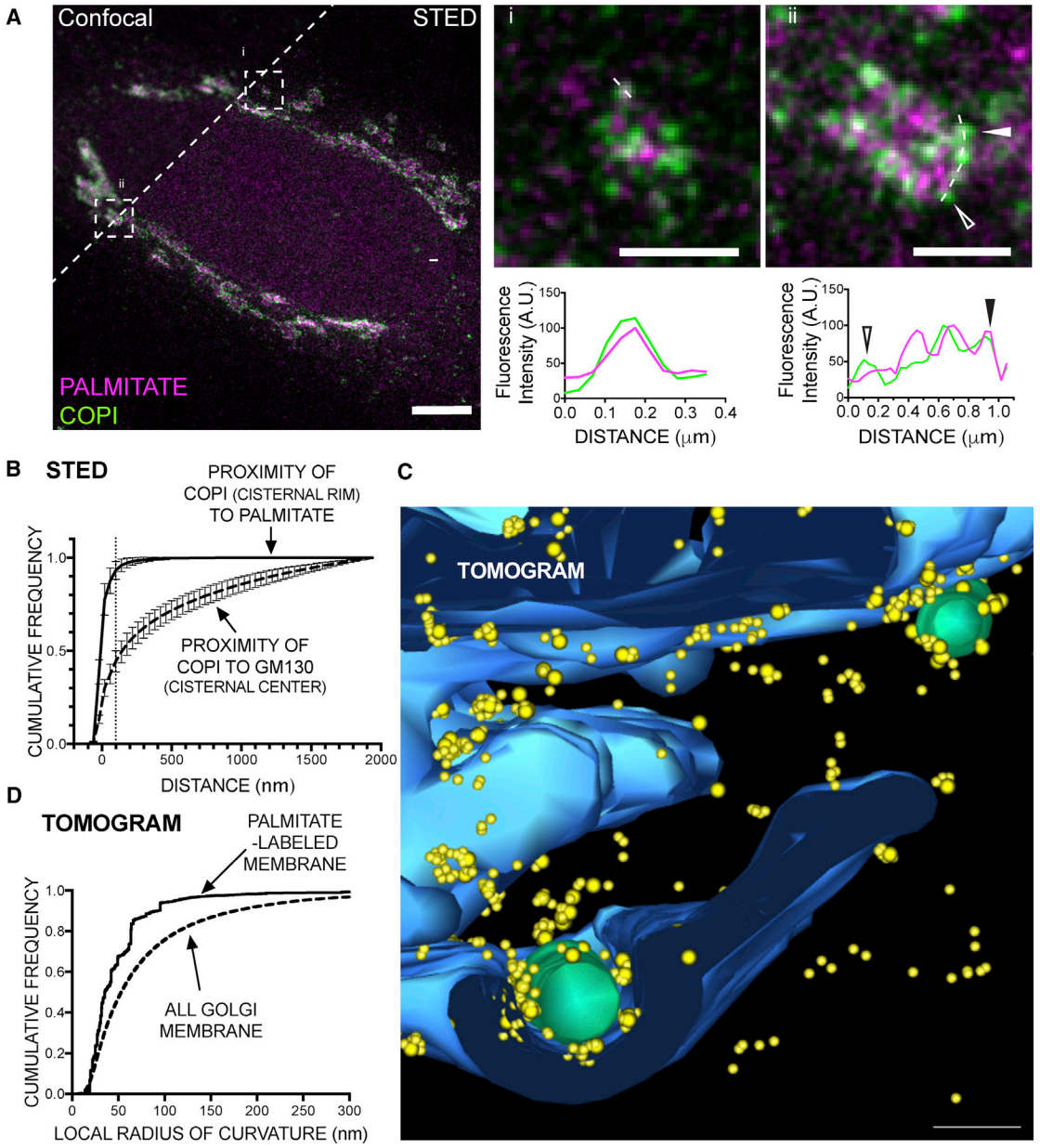

Figure 5. S-Palmitoylated Membrane Cargo Concentrates in Highly Curved Regions at the Cisternal Rims of the Golgi

(A) STED nanoscopy of S-palmitoylated proteins at the Golgi. doxSNAP-DHHC3 cells were induced for 5 hr and subsequently metabolically labeled with alkyne-palmitate for 20 min, followed by a 10-min chase in delipidated medium. After fixation and permeabilization, palmitoylated proteins were detected with azide-ATTO594, and coatomer or GM130 were immunolabeled with ATTO647N. Left: overview of Golgi area labeled for STED microscopy. Upper right: zoom into individual cisternal elements (dashes boxes i and ii). Lower right panel: line profiles obtained from the magnified images (dashed lines, arrowheads highlight the position of distinct COPI-clusters).

(B) Quantification of STED images (cumulative frequency distribution of the proximity of pixels) obtained from Golgi areas (dashed line: 100 nm; n = 10 Golgi areas per pair, mean and SD).

(C) Electron tomography of S-palmitoylated proteins at the Golgi. Expression of DHHC3 and labeling of the Golgi with alkyne-palmitate was performed as in (A) and followed by fixation and permeabilization of the cells. After click chemistry to azide-biotin, S-palmitoylated proteins were detected using streptavidin-fluoronanogold and subjected to double tilt electron tomography. 3D-modeling of the tomogram data was performed (Golgi membranes), and the loci of 3,575 gold-labeled palmitoylated proteins in the tomogram were annotated. Magnification of a cisternal rim area of palmitate-labeled Golgi membranes (3D tomogram model). Yellow: gold clusters (= palmitoylated proteins), blue: rendered Golgi membranes, green: vesicular or tubular structures; scale bar: 50 nm. Full model: Figure S6E.

(D) Local curvature was assessed at each point along the annotated membrane curves, and the cumulative frequency of total Golgi membrane curvature (dashed line) was compared to the underlying curvature observed in loci positive for S-palmitoylated proteins (solid line).

See also Figure S6.

To test this concept, we utilized a well-characterized system that allows intrinsic curvature preference to be directly measured when presented with a choice between a large vesicle and a small, highly curved, and contiguous tubule (Bo and Waugh, 1989). We expressed and purified from mammalian suspension cells a 54-amino-acid fragment of transferrin receptor consisting of the transmembrane helical domain flanked by juxta-membrane sequences at both ends (Figures 6A, S7A, and S7B). The peptide (termed "TfR mini") was prepared in both palmitoylated and de-palmitoylated (hydroxylamine-cleaved) forms (Figures S7C and S7D) and then reconstituted into giant unilamellar vesicles (GUVs). Tubules (Figure 6B) ranging from 20 to 150 nm in diameter can be pulled out from GUVs following adhesion of an applied micro-pipette tip (Bo and Waugh, 1989). TfR-mini, initially residing in the GUV, can then distribute at equilibrium between the curved tubule and the continuous, essentially planar GUV bilayer. The concentration of the TfR-mini in the tubule relative to the concentration remaining in the GUV can then be determined using established methods as can the tubule diameter (Bo and Waugh, 1989; Hochmuth et al., 1982; Sorre et al., 2009).

We observed that the transferrin receptor transmembrane domain was strongly concentrated in a palmitoylation-dependent manner into the tubules (Figures 6B and 6C). Enrichment increased progressively as the tubule diameter decreased (i.e., curvature increased). The greatest concentration occurred for diameters of curvature below 65 nm, and removing the attached palmitate groups abolished all curvature preference.

DISCUSSION

Mammalian Golgi cisternae are stacked due to the action of GRASP proteins, and it has been established that vesicle transport machinery (ARF1, COPI) preferentially accumulates at the highly curved rims of cisternae (Farquhar, 1985; Orci et al., 1986). Early electron microscopic studies of the distribution of VSV G within Golgi cisterna revealed a still-unexplained increase in the surface density of VSV G in the curved rims as compared to the flatter centers of the cisternae (Orci et al., 1986). The data presented here introduce a new concept to cell biology, and, in doing so, bear the potential to resolve a number of long-standing puzzles, including our own still-unexplained results from three decades ago that originally pointed to a palmitoyl transfer reaction from coA as an important determinant of COPI vesicle budding from Golgi cisterna.

The new idea is that membrane proteins—by virtue of acylation—acquire a preference for curved regions of the lipid bilayer and thus are spontaneously sorted toward the cisternal rim (Figure 7). In so doing, the palmitoylated proteins increase the rate of vesicle or tubule budding from these same regions by lowering the energy needed to further bend the local membrane to yield pinched-off carriers. The resultant diffusive flux (the gradient generated by removal of S-palmitoylated proteins from the rim) carries both non-acylated membrane as well as secretory cargo in the center of the cisternae toward the rim. This is supported by our observation that anterograde trafficking of the model cargos G and TfR is markedly accelerated across the Golgi (Figure 3) and that partitioning of bulk anterograde cargo is enhanced by maximizing the rate of palmitoylation through overexpression of DHHCs (Figures 4A–4C).

Deforming the membrane into a vesicle or tubule requires energy, typically provided by an externally applied shaping device such as a spherical or helical coat. This needed energy may also be provided from within the membrane if its constituent proteins intrinsically prefer high curvature. When such curvature-seeking proteins transit into regions of higher curvature, they lower the free energy of the system (applied device plus membrane), providing energy to drive the budding process. By reducing the activation energy for curving the membrane, curvature-seeking proteins will not only increase the rate of budding (vesicles or tubules) above the basal rate resulting from the external device alone but will themselves further concentrate into the budding membrane during the process. From a rate perspective, the optimal reaction will occur when the curvature preference of the membrane proteins considerably exceeds the physical curvature of the external membrane-shaping device. This is in agreement with our observation that the palmitoylated TfR transmembrane domain has a preference for bilayers with a diameter of curvature below 65 nm but lacks a curvature preference when it is not palmitoylated (Figure 6C). In comparison, the diameter of the vesicle enclosed in a COPI coat is about 70–80 nm (Orci et al., 1986), and a peripheral Golgi tubule has a diameter of 50 nm (Ladinsky et al., 1999).

A classical target sequence for palmitoylation of membrane proteins by DHHC family palmitoyltransferases simply appears to consist of one or more Cys residues close to the cytoplasmic end of the transmembrane domain (Aicart-Ramos et al., 2011). Based on our results, this simple motif might be considered as a sorting signal marking the cargo bearing it for rapid anterograde transport that is recognized by DHHCs in the *cis*-Golgi (Figures 1F and 1G) and actuated by attaching a fatty acid chain(s).

Although further detailed studies will be required, it appears that these straightforward concepts, originating from detailed analysis of the TfR and G protein, are likely to apply broadly to the anterograde-directed cargo in the Golgi. Notably, the bulk of palmitoyl acceptors in the Golgi membranes are cargo molecules (Figures 1B, 2B, and 2D) that transit the stack in the anterograde direction (Figures 1C, 1D, 2E, 2F, and S4E). As a class, these palmitoylated cargo demonstrate accelerated anterograde transport upon increasing the rate of their palmitoylation (Figures 2E, 2F, S3A, and S3B), and they localize to the curved rims of the Golgi (Figures 5B and 5C), strongly concentrating in regions whose local curvature is less than 50 nm (Figure 5D). As may be generalized from the physics governing the behavior of model S-palmitoylated transmembrane peptides (Figure 6), not only do palmitoylated anterograde cargo as a class partition into curved regions at the rims of the Golgi cisternae but producing more of them increases the proportion of the total Golgi surface that is in the very highly curved regions from which budding occurs (Figure S6G). In support of this view, a significant fraction of anterograde-targeted proteins (e.g., plasma membrane residents) are predicted by bioinformatics to be substrates for palmitoylation (Figures S3G and S3H). However, while we show that S-palmitoylation is a key new mechanism to promote anterograde traffic within the Golgi based on a membrane-intrinsic, physical-chemical process, this does not exclude other mechanisms that may augment sorting of cargo to the cisternal rim, e.g., hetero-oligomerization of S-palmitoylated

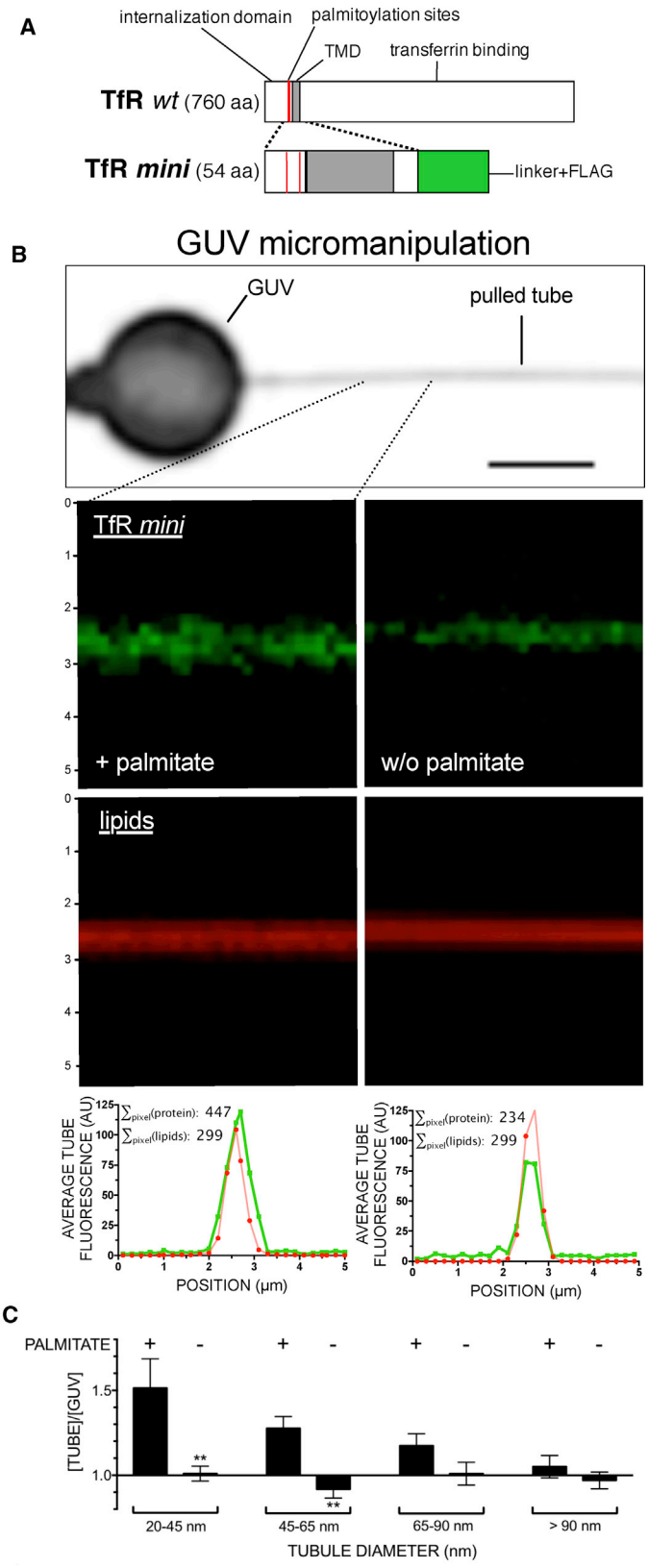

Figure 6. Curvature Preference May Be an Intrinsic Property of Palmitoylated Anterograde Cargo

(A) Schematic representation of a minimal construct of the transferrin receptor, TfRmini. Red: Cys residues 62 and 67; gray: transmembrane domain; green: linker and FLAG epitope.

(B) Micromanipulation of giant unilamellar vesicles (GUVs). GUVs containing biotinylated and fluorescently labeled lipids were formed, and recombinant proteins were reconstituted into GUVs. Next, two micropipettes were employed, one containing a streptavidin bead and one to exert suction on the GUV while pulling a tube out of the membrane due to the biotin-streptavidin interaction (upper panel). The ratio of the fluorescence of the recombinant protein in the tubule versus the GUV donor membrane divided by the intensity of membrane lipids in tubule versus the donor membrane was calculated (representative individual channels for S-palmitoylated or non-palmitoylated TfRmini: middle panels). The model tubes exhibit identical sum-of-lipid pixel intensities in the lipid channel and thus allow the direct comparison of sum of protein pixel intensities (lower panels; tube/GUV enrichment: +50% [S-palmitoylated TfRmini]; −20% [de-palmitoylated TfRmini]).

(C) S-palmitoylated TfRmini partitions into tubules with high curvature. TfRmini-containing GUVs were micromanipulated to generate different classes of tube diameters, and the relative excess of recombinant protein in the tube was plotted against increasing tube diameter bins for palmitoylated and de-palmitoylated (hydroxylamine-cleaved) TfRmini.

See also Figure S7.

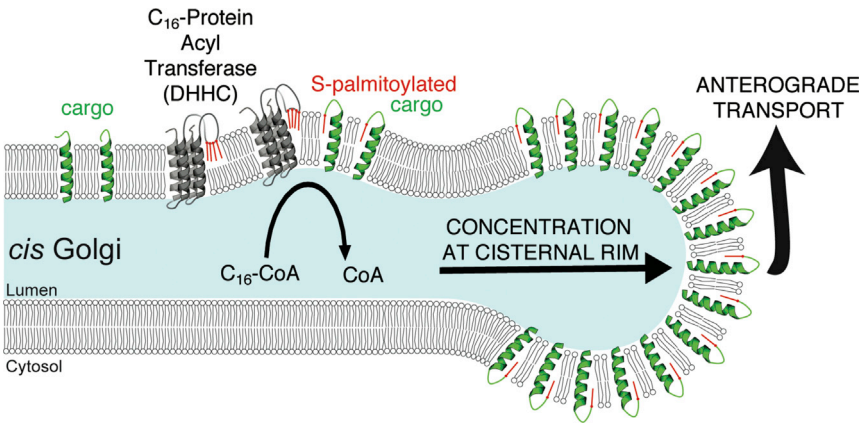

Figure 7. S-Palmitoylation Acts as a Sorting Signal for Anterograde Membrane Cargo at the *cis*-Golgi

Upon interaction with DHHCs in the *cis*-Golgi, anterograde membrane cargo is rapidly S-palmitoylated. This leads to an increased affinity for the highly positively curved cisternal rim, from which budding occurs, and an extraction of cargo from stacked (flat) Golgi membranes. Partitioning into curved regions at the rims of the Golgi cisternae increases the incorporation of S-palmitoylated proteins into coatomer-positive carriers, resulting in an acceleration of anterograde transport across the Golgi.

and non-palmitoylated cargo, protein folds that result in spontaneous curvature of the hydrophobic moiety (polytopic membrane proteins), or lectin-mediated interactions of S-palmitoylated membrane cargo with cargo in the lumen of the Golgi.

Why might palmitoylation of certain membrane proteins impart curvature preference? Acceptor Cys residues are frequently observed within a few amino acids of the cytoplasmic end of a transmembrane domain. This enables the fatty acid to insert into the cytoplasmic leaflet, adding surface area locally and changing the overall shape in the membrane (the diameter of a fatty acid in a liquid disordered phase is about 0.4 nm as compared to an α-helix of about 1.2 nm), thus being larger on the cytoplasmic than on the lumenal side. Anchoring a previously flexible local amino acid sequence to the cytoplasmic leaflet would convert it into a restricted loop-like extension of the transmembrane domain, further adding to the cone-like shape. This change in the shape (spontaneous curvature) now modulates the properties of the cargo so that it prefers highly curved regions of membrane, which in the Golgi stack are mainly present at the rims of the cisternae, thus concentrating the anterograde cargo in the regions where transport occurs. That intrinsic curvature preference causes partitioning to curved membranes is an established principle in membrane biochemistry (Frolov et al., 2011; Sheetz and Singer, 1974), and that S-palmitoylation can impact the spontaneous curvature of a membrane protein was recently demonstrated (Chlanda et al., 2017), supporting our proposed mechanism.

Our newly proposed physical-chemical way of thinking about anterograde transport in the Golgi might help explain many puzzling disparate observations. For example, we observed that VSV G protein appeared concentrated in the Golgi rims at every level of the stack (Orci et al., 1986). Second, overexpressing VSV G leads to an increase in the rate of transport accompanied by a dramatically increased prevalence of tubulation (i.e., curvature) at the rims (Trucco et al., 2004). Third, palmitoyl-CoA was known to dramatically accelerate the rate of budding of VSV G-containing COPI vesicles (and transport) in cell-free systems (Glick and Rothman, 1987; Pfanner et al., 1989; Ostermann et al., 1993).

In conclusion, we can envisage S-palmitoylation as the first example of a physical-chemical, membrane-intrinsic sorting process by which anterograde cargo spontaneously clusters within highly curved regions of the cisternal rim and to the exclusion of retrograde cargo and their receptors (Figure 7), thereby enabling their uptake into highly curved tubular (Trucco et al., 2004; CDC42-mediated: Park et al., 2015; ARF1-mediated: Bottanelli et al., 2017) or vesicular (COPI: Orci et al., 1986; Pellett et al., 2013; Rothman, 2014) carriers and thus resulting in an efficient net anterograde cargo transport.

STAR★METHODS

Detailed methods are provided in the online version of this paper and include the following:

- KEY RESOURCES TABLE
- CONTACT FOR REAGENT AND RESOURCE SHARING
- EXPERIMENTAL MODEL AND SUBJECT DETAILS
- METHOD DETAILS
  - Cell Culture and Reagents
  - Immunofluorescence, Ligand Labeling, Microscopy
  - Metabolic Labeling, Click Chemistry
  - Bioinformatics
  - Surface Biotinylation Assay
  - Lectin Assay
  - Electron Microscopy of *S*-Palmitoylated Proteins
  - Estimation of Membrane Curvature on Tomogram Data
  - Estimation of Proximities in STED Images
  - Purification of Recombinant Proteins from EXPI293 Cells
  - Identification of *S*-Palmitoylated Proteins
  - Micromanipulation of Proteo-Giant Unilamellar Vesicles
- QUANTIFICATION AND STATISTICAL ANALYSIS

SUPPLEMENTAL INFORMATION

Supplemental Information includes seven figures and one table and can be found with this article online at https://doi.org/10.1016/j.devcel.2018.10.024.

ACKNOWLEDGMENTS

This work was supported by the G. Harold and Leila Y. Mathers foundation (to J.E.R.), an NIH MIRA grant (GM118084; J.E.R.), and a postdoctoral fellowship of the Deutsche Forschungsgemeinschaft to A.M.E. We thank Al Mennone at

the Yale Center for Cellular and Molecular Imaging Facility (CCMI, NIH grant S10OD020142).

AUTHOR CONTRIBUTIONS

A.M.E., S.A.S., O.Z., F.B., H.Z., M.H., Z.X., F.R.-M., M.G., A.A.R., P.B., D.B., and F.P. analyzed data and performed experiments. A.M.E., D.T., D.B., F.P., and J.E.R. designed research, analyzed data, and provided conceptual input. A.M.E. and J.E.R. wrote the manuscript.

DECLARATION OF INTERESTS

The authors declare no competing interests.

Received: June 21, 2018
Revised: September 7, 2018
Accepted: October 20, 2018
Published: November 19, 2018

REFERENCES

Aicart-Ramos, C., Valero, R.A., and Rodriguez-Crespo, I. (2011). Protein palmitoylation and subcellular trafficking. Biochim. Biophys. Acta *1808*, 2981–2994.

Alvarez, E., Gironès, N., and Davis, R.J. (1990). Inhibition of the receptor-mediated endocytosis of diferric transferrin is associated with the covalent modification of the transferrin receptor with palmitic acid. J. Biol. Chem. *265*, 16644–16655.

Apolloni, A., Prior, I.A., Lindsay, M., Parton, R.G., and Hancock, J.F. (2000). H-ras but not K-ras traffics to the plasma membrane through the exocytic pathway. Mol. Cell. Biol. *20*, 2475–2487.

Bo, L., and Waugh, R.E. (1989). Determination of bilayer membrane bending stiffness by tether formation from giant, thin-walled vesicles. Biophys. J. *55*, 509–517.

Bergmann, J.E. (1989). Using temperature-sensitive mutants of VSV to study membrane protein biogenesis. Methods Cell Biol. *32*, 85–110.

Blanc, M., David, F., Abrami, L., Migliozzi, D., Armand, F., Bürgi, J., and van der Goot, F.G. (2015). SwissPalm: protein palmitoylation database. F1000Res. *4*, 261.

Bottanelli, F., Kromann, E.B., Allgeyer, E.S., Erdmann, R.S., Wood Baguley, S., Sirinakis, G., Schepartz, A., Baddeley, D., Toomre, D.K., Rothman, J.E., et al. (2016). Two-colour live-cell nanoscale imaging of intracellular targets. Nat. Commun. *7*, 10778.

Bottanelli, F., Kilian, N., Ernst, A.M., Rivera-Molina, F., Schroeder, L.K., Kromann, E.B., Lessard, M.D., Erdmann, R.S., Schepartz, A., Baddeley, D., et al. (2017). A novel physiological role for ARF1 in the formation of bidirectional tubules from the Golgi. Mol. Biol. Cell *28*, 1676–1678.

Charollais, J., and Van Der Goot, F.G. (2009). Palmitoylation of membrane proteins (review). Mol. Membr. Biol. *26*, 55–66.

Chien, A.J., Carr, K.M., Shirokov, R.E., Rios, E., and Hosey, M.M. (1996). Identification of palmitoylation sites within the L-type calcium channel β2a subunit and effects on channel function. J. Biol. Chem. *271*, 26465–26468.

Chlanda, P., Mekhedov, E., Waters, H., Sodt, A., Schwartz, C., Nair, V., Blank, P.S., and Zimmerberg, J. (2017). Palmitoylation contributes to membrane curvature in influenza A virus assembly and hemagglutinin-mediated membrane fusion. J. Virol. *91*. https://doi.org/10.1128/JVI.00947-17.

Coleman, R.A., Rao, P., Fogelsong, R.J., and Bardes, E.S.G. (1992). 2-bromopalmitoyl-CoA and 2-bromopalmitate: promiscuous inhibitors of membrane-bound enzymes. Biochim. Biophys. Acta *1125*, 203–209.

Demers, A., Ran, Z., Deng, Q., Wang, D., Edman, B., Lu, W., and Li, F. (2014). .Palmitoylation is required for intracellular trafficking of influenza B virus NB protein and efficient influenza B virus growth in vitro. J. Gen. Virol. *95*, 1211–1220.

Du, K., Murakami, S., Sun, Y., Kilpatrick, C.L., and Luscher, B. (2017). DHHC7 Palmitoylates glucose transporter 4 (Glut4) and regulates Glut4 membrane translocation. J. Biol. Chem. *292*, 2979–2991.

Duden, R., Griffiths, G., Frank, R., Argos, P., and Kreis, T.E. (1991). Beta-COP, a 110 KD protein associated with non-clathrin-coated vesicles and the Golgi complex, shows homology to beta-adaptin. Cell *64*, 649–665.

El-Husseini, Ael-D., Schnell, E., Dakoji, S., Sweeney, N., Zhou, Q., Prange, O., Gauthier-Campbell, C., Aguilera-Moreno, A., Nicoll, R.A., and Bredt, D.S. (2002). Synaptic strength regulated by palmitate cycling on PSD-95. Cell *108*, 849–863.

Farquhar, M.G. (1985). Progress in unraveling pathways of Golgi traffic. Annu. Rev. Cell Biol. *1*, 447–488.

Frolov, V.A., Shnyrova, A.V., and Zimmerberg, J. (2011). Lipid polymorphisms and membrane shape. Cold Spring Harb. Perspect. Biol. *3*, a004747.

Fukata, M., Fukata, Y., Adesnik, H., Nicoll, R.A., and Bredt, D.S. (2004). Identification of PSD-95 palmitoylating enzymes. Neuron *44*, 987–996.

Fukata, Y., and Fukata, M. (2010). Protein palmitoylation in neuronal development and synaptic plasticity. Nat. Rev. Neurosci. *11*, 161–175.

Glick, B.S., and Rothman, J.E. (1987). Possible role for fatty acyl-coenzyme A in intracellular protein transport. Nature *326*, 309–312.

Gonzalo, S., and Linder, M.E. (1998). SNAP-25 palmitoylation and plasma membrane targeting require a functional secretory pathway. Mol. Biol. Cell *9*, 585–597.

Gottlieb, C.D., Zhang, S., and Linder, M.E. (2015). The cysteine-rich domain of the DHHC3 palmitoyltransferase is palmitoylated and contains tightly bound zinc. J. Biol. Chem. *290*, 29259–29269.

Greaves, J., and Chamberlain, L.H. (2011). DHHC palmitoyl transferases: substrate interactions and (patho) physiology. Trends Biochem. Sci. *36*, 245–253.

Greaves, J., Munro, K.R., Davidson, S.C., Riviere, M., Wojno, J., Smith, T.K., Tomkinson, N.C., and Chamberlain, L.H. (2017). Molecular basis of fatty acid selectivity in the zDHHC family of S-acyltransferases revealed by click chemistry. Proc. Natl. Acad. Sci. USA *114*, E1365–E1374.

Greaves, J., Salaun, C., Fukata, Y., Fukata, M., and Chamberlain, L.H. (2008). .Palmitoylation and membrane interactions of the neuroprotective chaperone cysteine-string protein. J. Biol. Chem. *283*, 25014–25026.

Hochmuth, R.M., Wiles, H.C., Evans, E.A., and McCown, J.T. (1982). Extensional flow of erythrocyte membrane from cell body to elastic tether. II. Experiment. Biophys. J. *39*, 83–89.

Jennings, B.C., and Linder, M.E. (2012). DHHC protein S-acyltransferases use similar ping-pong kinetic mechanisms but display different acyl-CoA specificities. J. Biol. Chem. *287*, 7236–7245.

Kolb, H.C., Finn, M.G., and Sharpless, K.B. (2001). Click chemistry: diverse chemical function from a few good reactions. Angew. Chem. Int. Ed. *40*, 2004–2021.

Ladinsky, M.S., Mastronarde, D.N., McIntosh, J.R., Howell, K.E., and Staehelin, L.A. (1999). Golgi structure in three dimensions: functional insights from the normal rat kidney cell. J. Cell Biol. *144*, 1135–1149.

Linder, M.E., and Deschenes, R.J. (2007). Palmitoylation: policing protein stability and traffic. Nat. Rev. Mol. Cell Biol. *8*, 74–84.

Lobo, S., Greentree, W.K., Linder, M.E., and Deschenes, R.J. (2002). Identification of a Ras palmitoyltransferase in Saccharomyces cerevisiae. J. Biol. Chem. *277*, 41268–41273.

Magee, A.I., Koyama, A.H., Malfer, C., Wen, D., and Schlesinger, M.J. (1984). .Release of fatty acids from virus glycoproteins by hydroxylamine. Biochim. Biophys. Acta *798*, 156–166.

Mathivet, L., Cribier, S., and Devaux, P.F. (1996). Shape change and physical properties of giant phospholipid vesicles prepared in the presence of an AC electric field. Biophys. J. *70*, 1112–1121.

Mitchell, D.A., Mitchell, G., Ling, Y., Budde, C., and Deschenes, R.J. (2010). Mutational analysis of Saccharomyces cerevisiae Erf2 reveals a two-step reaction mechanism for protein palmitoylation by DHHC enzymes. J. Biol. Chem. *285*, 38104–38114.

Nielsen, H. (2017). Predicting secretory proteins with SignalP. Methods Mol. Biol. *1611*, 59–73.

Ohno, Y., Kihara, A., Sano, T., and Igarashi, Y. (2006). Intracellular localization and tissue-specific distribution of human and yeast DHHC cysteine-rich domain-containing proteins. Biochim. Biophys. Acta *1761*, 474–483.

Omura, S., Tomoda, H., Xu, Q.M., Takahashi, Y., and Iwai, Y. (1986). Triacsins, new inhibitors of acyl-CoA synthetase produced by Streptomyces sp. J. Antibiot. *39*, 1211–1218.

Orci, L., Glick, B.S., and Rothman, J.E. (1986). A new type of coated vesicular carrier that appears not to contain clathrin: its possible role in protein transport within the Golgi stack. Cell *46*, 171–184.

Ostermann, J., Orci, L., Tani, K., Amherdt, M., Ravazzola, M., Elazar, Z., and Rothman, J.E. (1993). Stepwise assembly of functionally active transport vesicles. Cell *75*, 1015–1025.

Palmer, D.J., Helms, J.B., Beckers, C.J., Orci, L., and Rothman, J.E. (1993). Binding of coatomer to Golgi membranes requires ADP-ribosylation factor. J. Biol. Chem. *268*, 12083–12089.

Park, S.Y., Yang, J.S., Schmider, A.B., Soberman, R.J., and Hsu, V.W. (2015). Coordinated regulation of bidirectional COPI transport at the Golgi by CDC42. Nature *521*, 529–532.

Pellett, P.A., Dietrich, F., Bewersdorf, J., Rothman, J.E., and Lavieu, G. (2013). Inter- Golgi transport mediated by COPI-containing vesicles carrying small cargoes. Elife *2*, e01296.

Percher, A., Ramakrishnan, S., Thinon, E., Yuan, X., Yount, J.S., and Hang, H.C. (2016). Mass-tag labeling reveals site-specific and endogenous levels of protein S-fatty acylation. Proc. Natl. Acad. Sci. USA *113*, 4302–4307.

Peters, C., Tsirigos, K.D., Shu, N., and Elofsson, A. (2016). Improved topology predictions using the terminal hydrophobic helices rule. Bioinformatics *32* (8), 1158–1162.

Pfanner, N., Orci, L., Glick, B.S., Amherdt, M., Arden, S.R., Malhotra, V., and Rothman, J.E. (1989). Fatty acyl-coenzyme A is required for budding of transport vesicles from Golgi cisternae. Cell *59*, 95–102.

Politis, E.G., Roth, A.F., and Davis, N.G. (2005). Transmembrane topology of the protein palmitoyl transferase Akr1. J. Biol. Chem. *280*, 10156–10163.

Presley, J.F., Cole, N.B., Schroer, T.A., Hirschberg, K., Zaal, K.J., and Lippincott-Schwartz, J. (1997). ER-to-Golgi transport visualized in living cells. Nature *389*, 81–85.

Rana, M.S., Kumar, P., Lee, C.J., Verardi, R., Rajashankar, K.R., and Banerjee, A. (2018). Fatty acyl recognition and transfer by an integral membrane S-acyltransferase. Science *359*, 6372, eaao6326.

Ren, J., Wen, L., Gao, X., Jin, C., Xue, Y., and Yao, X. (2008). CSS-palm 2.0: an updated software for palmitoylation sites prediction. Protein Eng. Des. Sel. *21*, 639–644.

Rose, J.K., Adams, G.A., and Gallione, C.J. (1984). The presence of cysteine in the cytoplasmic domain of the vesicular stomatitis virus glycoprotein is required for palmitate addition. Proc. Natl. Acad. Sci. USA *81*, 2050–2054.

Roth, A.F., Feng, Y., Chen, L., and Davis, N.G. (2002). The yeast DHHC cysteine-rich domain protein Akr1p is a palmitoyl transferase. J. Cell Biol. *159*, 23–28.

Rothman, J.E. (2014). The principle of membrane fusion in the cell (nobel lecture). Angew. Chem. Int. Ed. *53*, 12676–12694.

Salaun, C., Greaves, J., and Chamberlain, L.H. (2010). The intracellular dynamic of protein palmitoylation. J. Cell Biol. *191*, 1229–1238.

Schmidt, M.F., and Schlesinger, M.J. (1979). Fatty acid binding to vesicular stomatitis virus glycoprotein: a new type of post-translational modification of the viral glycoprotein. Cell *17*, 813–819.

Sheetz, M.P., and Singer, S.J. (1974). Biological membranes as bilayer couples. A molecular mechanism of drug-erythrocyte interactions. Proc. Natl. Acad. Sci. USA *71*, 4457–4461.

Smotrys, J.E., and Linder, M.E. (2004). Palmitoylation of intracellular signaling proteins: regulation and function. Annu. Rev. Biochem. *73*, 559–587.

Sorre, B., Callan-Jones, A., Manneville, J.B., Nassoy, P., Joanny, J.F., Prost, J., Goud, B., and Bassereau, P. (2009). Curvature-driven lipid sorting needs proximity to a demixing point and is aided by proteins. Proc. Natl. Acad. Sci. USA *106*, 5622–5626.

Taylor, J.A., Limbrick, A.R., Allan, D., and Judah, J.D. (1984). Isolation of highly purified Golgi membranes from rat liver. Use of cycloheximide in vivo to remove Golgi contents. Biochim. Biophys. Acta *769*, 171–178.

Todorow, Z., Spang, A., Carmack, E., Yates, J., and Schekman, R. (2000). Active recycling of yeast Golgi mannosyltransferase complexes through the endoplasmic reticulum. Proc. Natl. Acad. Sci. USA *97*, 13643–13648.

Trucco, A., Polishchuk, R.S., Martella, O., Di Pentima, A., Fusella, A., Di Giandomenico, D., San Pietro, E., Beznoussenko, G.V., Polishchuk, E.V., Baldassarre, M., et al. (2004). Secretory traffic triggers the formation of tubular continuities across Golgi sub-compartments. Nat. Cell Biol. *6*, 1071–1081.

STAR★METHODS

KEY RESOURCES TABLE

REAGENT or RESOURCE	SOURCE	IDENTIFIER
Antibodies		
Rabbit polyclonal anti-GPP130	BioLegend	Cat# 923801
Mouse monoclonal anti-p230	BD Transduction Laboratories	Cat# 611281
Rabbit anti-SNAP tag	New England BioLabs	Cat# P9310S
Rabbit anti-HALO tag	Promega	Cat# G9281
Mouse monoclonal anti-FLAG	Sigma-Aldrich	Cat# F1804
Rabbit anti-GFP	Abcam	Cat# ab6556
Mouse anti-GM130	BD Transduction Laboratories	Cat# 610823
Mouse anti-TGN46	Abcam	Cat# ab2809
Mouse anti-betaCOP	Palmer et al. (1993)	CM1
Mouse anti-betaCOP	Duden et al. (1991)	BetaEAGE
Goat anti-mouse IgG (H+L), Highly Cross-Absorbed Secondary Antibody, Alexa Fluor 488	Thermo Fisher Scientific	Cat# A32723
Goat anti-rabbit IgG (H+L), Highly Cross-Absorbed Secondary Antibody, Alexa Fluor 488	Thermo Fisher Scientific	Cat# A11034
Goat anti-rabbit IgG (H+L), Highly Cross-Absorbed Secondary Antibody, Alexa Fluor 568	Thermo Fisher Scientific	Cat# A11036
Goat anti-mouse IgG (H+L), Highly Cross-Absorbed Secondary Antibody, Alexa Fluor 568	Thermo Fisher Scientific	Cat# A11031
Goat anti-mouse IgG (H+L), Highly Cross-Absorbed Secondary Antibody, Alexa Fluor 647	Thermo Fisher Scientific	Cat# A21236
Goat anti-rabbit IgG (H+L), Highly Cross-Absorbed Secondary Antibody, Alexa Fluor 647	Thermo Fisher Scientific	Cat# A21245
Anti-FLAG M2 affinity Gel	Sigma-Aldrich	Cat# A2220
Anti-Mouse-IgG - Atto647N	Sigma-Aldrich	Cat# 50185
IRDye 680RD Goat-anti-Rabbit IgG (H+L)	LI-COR	Cat# 925-68072
Bacterial and Virus Strains		
Subcloning Efficiency™ DH5α™ Competent Cells	Thermo Fisher Scientific	Cat# 18265017
Chemicals, Peptides, and Recombinant Proteins		
Palmitic Acid Alkyne	Cayman Chemical	Cat# 13266
Myristic Acid Alkyne	Cayman Chemical	Cat# 13267
17-Octadecynoic Acid	Cayman Chemical	Cat# 90270
Alexa Fluor 488 Azide	Thermo Fisher Scientific	Cat# A10266
Click-IT™ Palmitic Acid, Azide	Thermo Fisher Scientific	Cat# C10265
Alexa Fluor 647 Azide	Thermo Fisher Scientific	Cat# A10277
Biotin Azide	Thermo Fisher Scientific	Cat# B10184
Atto 594 Azide	Atto-Tec	Cat# AD594-101
FluoroNanogold Streptavidin	Nanoprobes	Cat# 7216
Lectin HPA, Alexa Fluor 647	Thermo Fisher Scientific	Cat# L32454
Jacalin Agarose	Thermo Fisher Scientific	Cat# 20395
Alexa Fluor 488 NHS Ester	Thermo Fisher Scientific	Cat# A20000
Alexa Fluor 647 NHS Ester	Thermo Fisher Scientific	Cat# A37573
EZ-Link Sulfo-NHS-Biotin	Thermo Fisher Scientific	Cat# A39256
Fetal Bovine Serum, charcoal stripped	Thermo Fisher Scientific	Cat# A3382101
Fetal Bovine Serum	Thermo Fisher Scientific	Cat# A10270106
FuGENE HD Transfection Reagent	Promega	Cat# E2311

(*Continued on next page*)

Continued

REAGENT or RESOURCE	SOURCE	IDENTIFIER
ProLong Gold Antifade Mountant	Thermo Fisher Scientific	Cat# P36934
Opti-MEM Reduced Serum Medium	Thermo Fisher Scientific	Cat# 31985070
ExpiFectamine 293 Transfection Kit	Thermo Fisher Scientific	Cat# A14524
Expi293 Expression Medium	Thermo Fisher Scientific	Cat# A1435102
FLAG tag Peptide	Sigma-Aldrich	Cat# F3290
SNAP-Cell 505-Star	New England BioLabs	Cat# S9103S
SNAP-Cell 647-SiR	New England BioLabs	Cat# S9102S
SNAP-Cell TMR-Star	New England BioLabs	Cat# S9105S
HaloTag Alexa Fluor 488	Promega	Cat# G1001
HaloTag TMRDirect	Promega	Cat# G2991
2-Bromohexadecanoic acid	Sigma-Aldrich	Cat# 238422
Triacsin C	Cayman Chemical	Cat# 10007448
Palmostatin B	Millipore Sigma	Cat# 508738
Cycloheximide	Sigma-Aldrich	Cat# C4859
DOPC	Avanti	Cat# 850375
DOPE	Avanti	Cat# 850725
DSPE-PEG-biotin	Avanti	Cat# 880129
DOPE-Atto 488	Atto-Tec	Cat# AD 488-161
D/D Solubilizer	Takara	Cat# 635054
Neutravidin-Agarose	Thermo Fisher Scientific	Cat# 29200
Critical Commercial Assays		
Click-iT Cell Reaction Buffer Kit	Thermo Fisher Scientific	Cat# C10269
EndoH	New England BioLabs	Cat# P0702S
NuPAGE 4-12% Bis-Tris Precast Protein Gels	Thermo Fisher Scientific	Cat# NP0321BOX
Deposited Data		
Scipy toolkit	www.python-microscopy.org	Python-microscopy package
Experimental Models: Cell Lines		
HeLa Cell Line	ATCC	Cat# HeLa ATCC CCL-2
Expi293F Cells	Thermo Fisher Scientific	Cat# 14527
HeLa-(tet-on)-SNAPf-hzDHHC3	This paper	N/A
Oligonucleotides		
Primers for cloning, see Table S1	This paper	N/A
Recombinant DNA		
pEF-Bos-HA mouse DHHC isoforms 1-23	Fukata et al. (2004)	N/A
pCMV6-Entry-hzDHHC-3	OriGene	Cat# RC215095
pCMV6-Entry-hzDHHC-7	OriGene	Cat# RC227047
pCMV6-Entry-hzDHHC-9	OriGene	Cat# RC200083
pCMV6-Entry-hzDHHC-11	OriGene	Cat# RC204383
pCMV6-Entry-hzDHHC-13	OriGene	Cat# RC208925
pCMV6-Entry-hzDHHC-15	OriGene	Cat# RC228259
pCMV6-Entry-hzDHHC-17	OriGene	Cat# RC207982
pCMV6-Entry-hzDHHC-21	OriGene	Cat# RC207295
pCMV6-Entry-hzDHHC-22	OriGene	Cat# RC212063
VSV G-3-GFP	Presley et al. (1997)	Addgene plasmid # 11912
pCW57.1	David Root	Addgene plasmid # 41393
VSV G-C490A-GFP	This paper	N/A
pTfR-FM4-Halo	Bottanelli et al. (2016)	N/A
pTfR-C62AC67A-FM4-Halo	This paper	N/A

(*Continued on next page*)

Continued

REAGENT or RESOURCE	SOURCE	IDENTIFIER
pCMV-TfRmini-FLAG	This paper	N/A
pSNAPf-hzDHHC3	This paper	N/A
pSNAPf-hzDHHS3	This paper	N/A
pSNAPf-hzDHHC7	This paper	N/A
pSNAPf-hzDHHS7	This paper	N/A
pSNAPf-hzDHHC9	This paper	N/A
pSNAPf-hzDHHC11	This paper	N/A
pSNAPf-hzDHHC13	This paper	N/A
pSNAPf-hzDHHC15	This paper	N/A
pSNAPf-hzDHHC17	This paper	N/A
pC4S1-FM4-FCS-hGH	Takara	N/A
Software and Algorithms		
Volocity	Quorum Technologies	http://quorumtechnologies.com/index.php/component/content/article/31-volocity-software/31-volocity-quantitation
Image Studio	Li-Cor	https://www.licor.com/bio/products/software/image_studio/?gclid=CjwKCAjw2rjcBRBuEiwAheKeLwilkBK03BHIuadi0W5pKGMVVTqk48YavpC3J-vsxUnoB7OemRQyjxoCVnMQAvD_BwE
Prism 6	Graphpad	https://www.graphpad.com/scientific-software/prism/
ImageJ 1.52c	NIH	https://imagej.nih.gov/ij/

CONTACT FOR REAGENT AND RESOURCE SHARING

Further information and requests for resources and reagents should be directed to and will be fulfilled by the Lead Contact, Andreas M. Ernst (andreas.ernst@yale.edu).

EXPERIMENTAL MODEL AND SUBJECT DETAILS

HeLa cells were maintained at 37°C in 5 % CO_2 in DMEM (Gibco, Grand Island, NY, United States) supplemented with 10 % FBS (Gibco). EXPI293F cells (Thermo Fisher Scientific) were maintained at 37°C in 8 % CO_2 in Expi293 expression medium (Thermo Fisher Scientific). A stably transfected, doxycycline-inducible SNAP-hDHHC3 HeLa cell line was generated employing pCW57.1 (a gift from David Root, Addgene plasmid #41393) and SNAP-DHHC3 plasmid.

METHOD DETAILS

Cell Culture and Reagents

HeLa cells were maintained at 37°C in 5 % CO_2 in DMEM (Gibco, Grand Island, NY, United States) supplemented with 10 % FBS (Gibco). Plasmid transfections were performed with Fugene HD (Promega, Madison, WI, USA) as recommended by the manufacturer. Release of FM4-domain-containing constructs from the ER was performed with the disaggregating drug D/D solubilizer (Clontech, Mountain View, CA, USA) at a final concentration of 1.5 μM. HA-tagged mouse zDHHC constructs were gift from Y. Fukata and M. Fukata (Fukata et al., 2004). Human DHHC cDNA clones isoforms 3, 7, 9, 11, 13, 15, 17, 21, and 22 were obtained from Origene (Rockville, MD, USA), and subcloned to pSNAPf plasmids (NEB, Ipswich, MA, USA). (tsO45)VSV G-3-GFP and TfR-FM4-HALO were a gift from Derek Toomre (Yale). SNAP-tag ligands (benzylguanine-conjugates) were purchased from NEB. Live-cell imaging and temperature blocks were performed in in HEPES-buffered imaging medium supplemented with 20 mM glucose (Molecular Probes, Eugene, OR, U.S.A) and in temperature-controlled incubators. EndoH assay kit was purchased from Promega and used according to the instructions of the manufacturer. Jacalin-agarose was purchased from Thermo Fisher.

Cycloheximide (final C: 100 μg/ml), 2-bromopalmitate (final C: 100 μM), and Triacsin C (final C: 100 μM) were obtained from Sigma-Aldrich (St. Louis, MO, U.S.A), palmostatin B from Merck Millipore (Darmstadt, Germany).

Immunofluorescence, Ligand Labeling, Microscopy

For imaging experiments, 100,000 HeLa cells were seeded on glass-bottom dishes (MatTek, Ashland, MA, USA) 24 h prior to transfection. Live-cell labeling of SNAP- and HALO-tagged proteins was performed for 1h at a final concentration of 5 μM, followed by three washes in medium and a subsequent additional incubation in medium for 30 min. The cells were either imaged live (in HEPES-buffered imaging solution (Gibco, Grand Island, NY, United States) supplemented with 0.1% FBS), or chemically fixed in 4 % paraformaldehyde in PBS for 10 min at RT as indicated. Cells were then permeabilized in permeabilization buffer (0.3 % NP-40, 0.05 % Triton X-100, 0.1 % BSA (IgG free), 1X PBS) for 2 min at RT, washed three times in wash buffer (0.05 % NP-40, 0.05 % Triton X-100, 0.2 % BSA (IgG free), 1X PBS), and subsequently blocked in blocking buffer (0.05 % NP-40, 0.05 % Triton X-100, 5 % goat serum, 1X PBS) for 1h. Primary antibodies were diluted at 1:500 in blocking buffer, and added to cells for 1h at RT. Next, the cells were washed three times in wash buffer (0.05 % NP-40, 0.05 % Triton X-100, 0.2 % BSA (IgG free), 1X PBS), incubated with a dilution of a fluorophore-labeled secondary antibody (1:1000) in blocking buffer for 1 h at RT, washed three times with wash buffer, and twice in PBS. The cells were mounted with ProLong Gold antifade reagent (Life Technologies, Carlsbad, CA) and 1 mm thick precleaned microscope slides (Thermo Fisher Scientific, Waltham, MA). Antibodies: anti-GPP130 (BioLegend, San Diego, CA, USA), anti-p230 (BD Biosciences, San Jose, CA, USA), anti-betaCOP (CM1, Palmer et al., 1993 and BetaEAGE, Duden et al., 1991), GM130 BD Transduction Laboratories, Franklin Lakes, NJ, U.S.A). All secondary antibodies conjugated to fluorescent dyes were purchased from Thermo Fisher (Waltham, MA, USA). Confocal imaging was performed on a Zeiss LSM710duo microscope with a 63x oil objective. TIRF imaging was performed on a DeltaVision OMX (Little Chalfont, UK). 3D-structured illumination (SIM) imaging was performed on a DeltaVision OMX (Little Chalfont, UK). STED imaging was carried out on a commercial Leica TCS SP8 STED 3X equipped with a white light excitation source. Excitation wavelengths: 594 and 650 nm. For detection HyD 1 and HyD 2 were set to 604- to 644- and 665- to 705-nm windows. The 775-nm depletion laser was used for both ATTO594 and ATTO647N. The two colors were imaged sequentially line by line. Image quantifications (Pearson's R, integrated intensity, line profiles) were performed in ImageJ and Volocity software (PerkinElmer, Waltham, MA, U.S.A).

Metabolic Labeling, Click Chemistry

Alkyne-functionalized fatty acid analogues were obtained from Cayman (Ann Arbor, MI, USA), azide-palmitate was obtained from Thermo Fisher, and lipid stocks were kept at 10 mM in ethanol and at -20°C. For metabolic labeling reactions, the lipid analogues were added to delipidated medium (DMEM + 10% charcoal-stripped FBS, Thermo Fisher), sonicated, incubated at 37°C for 10 min, and added at a final concentration of 50 μM to 70%-confluent HeLa cells. CuAAC (Copper(I)-catalyzed Azide-Alkyne Cycloaddition) was performed using the Cell reaction kit from Thermo Fisher (Waltham, MA, USA) according to the manufacturer. Azide- and alkyne- conjugated dyes were obtained from Thermo Fisher and used at a final concentration of 5 μM. After CuAAC, unreacted dye was removed with 2% (w/v) of delipidated BSA in PBS for 1h. For in-gel fluorescence, HeLa cells were labeled with the functionalized lipid analogues for 20 minutes in delipidated medium. The cells were scraped, sonicated on a microtip sonicator for 10 s, and subjected to CuAAC to azide-AF647. The samples were lysed in 50 mM HEPES/KOH, 150 mM NaCl, 1% (v/v) TX-100, sonicated, subjected to chloroform-methanol precipitation and dried in a speed-vac. Pellets were either treated with neutral hydroxylamine or 50mM HEPES/KOH, 150mM NaCl, and re-precipitated. Finally, the pellets were resuspended in 6x protein samples buffer (16% SDS), subjected to SDS-PAGE, and scanned on an infrared imager (LI-COR Odyssey; Lincoln, NE, USA). Hydroxylamine-cleavage of thioesters in microscopy samples was performed at 1.5 M in PBS (pH 7.2) for 2 h, and extensively washed with PBS containing 0.05 % Triton X-100 prior to imaging.

Bioinformatics

All reviewed human proteins annotated as membrane proteins were downloaded from Uniprot, and three datasets that correspond to different subcellular compartments (ER, Golgi, plasma membrane) were generated, and only proteins annotated as having experimentally verified subcellular locations were used in the study. The css-palm sites were predicted using CSS-Palm 2.0 (Ren et al., 2008). In order to find the inner loops of the proteins we used scampi 2.0 together with SignalP4.0 (Peters et al., 2016; Nielsen, 2017).

Surface Biotinylation Assay

HeLa cells grown in 6-well plates to 50% confluency were transfected using 1 μg of the respective plasmid DNA and 3 μl of Fugene HD transfection reagent (Promega) for 24 h. Cells were washed twice in PBS Ca/Mg (PBS with 1 mM $MgCl_2$, 0.1 mM $CaCl_2$) and subsequently incubated in 600 μl/well of a 500 μg/ml sulfo-NHS-biotin solution (Pierce, buffer: 150 mM NaCl, 10 mM triethanolamine pH 9.0, 2 mM $CaCl_2$, freshly prepared) for 30 min on ice. The cells were then washed in quenching buffer (PBS Ca/Mg, 100 mM glycine), and incubated in 600 μl/well of quenching buffer for 20 min on ice. The cells were washed twice with PBS (without Mg/Ca) and incubated for 10 min with 300 μl of lysis buffer (50 mM HEPES–NaOH, pH 7.4, 100 mM NaCl, 5 mM EDTA, 1% (v/v) Triton X-100, 0.5% (w/v) deoxycholate, and protease inhibitor cocktail (Roche)). Cells were scraped, transferred to Eppendorf tubes and sonicated for 3 min. Next, the tubes were incubated for 15 min with constant agitation at RT. Finally, the lysate was centrifuged for 10 min at 13 000 rpm and 4°C, and the supernatant was retained. 40 μl of Neutravidin-coupled beads (Thermo Fisher) were washed twice with 300 μl of lysis buffer. Centrifugation steps with beads were performed for 1 min at 3000×*g* and 4°C. The retained supernatant was then added to the beads and placed on a rotor wheel for 1 h at RT. Samples were eluted with 6× SDS-sample buffer (16% SDS) for 10 min at 95°C. Eluates were obtained after brief centrifugation at 16 000×*g* and RT. Input (lysate, 2.5% of total) and eluates (25% of total) were subjected to SDS–PAGE (Bis–Tris 4–12% gradient gels, Invitrogen) in MES buffer (Invitrogen), and

transferred to PVDF membranes via wet blot at 100 V for 1 h. The blots were decorated with anti-rabbit-IRdye680 coupled antibodies (Li-Cor) and analyzed on a LI-COR Odyssey device. Signal intensities were quantified using Li-Cor software.

Lectin Assay

HeLa cells grown in 10 cm dishes were grown to 50% confluency were transfected using 3 μg of the respective plasmid DNA and 9 μl of Fugene HD transfection reagent (Promega) for 24 h. After release of the cargos from the ER (temperature shift or D/D solubilizer) for the indicated times, the cells were scraped in 300 μl PBS containing protease inhibitors (Roche), pelleted at 16,000xg and resuspended 300 μl of lysis buffer (50 mM HEPES–NaOH, pH 7.4, 100 mM NaCl, 5 mM EDTA, 1% (v/v) Triton X-100, 0.5% (w/v) deoxycholate, and protease inhibitor cocktail (Roche)), and sonicated with a microtip sonicator for 10s, amplitude 15. The lysate was centrifuged for 8 min at 3,000xg and 4°C, and the supernatant was retained. 50 μl of Jacalin-coupled agarose was used per lysate. After 3 washes in lysis buffer, lysates were added to the beads and placed on a rotor wheel for 1 h at RT. After 3 washes in lysis buffer, the samples were eluted with 6× SDS-sample buffer (16% SDS) for 10 min at 95°C. Eluates were obtained after brief centrifugation at 16 000×*g* and RT and subjected to Western blot.

Electron Microscopy of *S*-Palmitoylated Proteins

doxSNAP-DHHC3 HeLa cells were plated in MatTek dishes and grown to 80% confluency. Expression of DHHC3 was induced by adding a final concentration of 2.5μg/ml doxycycline (Sigma-Aldrich) for 5 h. Next, the cells were metabolically labeled with 50 μM alkyne-palmitate for the indicated times, washed with delipidated medium, and fixed with 2% gluteraldehyde/0.1M sodium cacodylate buffer for 1 h RT. The samples were rinsed in cacodylate buffer for 30 minutes, and subsequently PBS containing 5% charcoal stripped serum for 4 hours with repeated exchanges to remove residual glutaraldehyde. Next, the cells were permeabilized for 1 h in 0.1% saponin-containing blocking buffer (see immunofluorescence, without TX100 and NP40). Next, CuAAC to azide-PEG4-biotin was performed for 30 min RT, and the cells were repeatedly rinsed with PBS containing 5% charcoal stripped serum for 1 h, RT. Finally, the cells were incubated with 10ug/ml streptavidin-fluronanogold 488 (Nanoprobes, Yaphank, NY, USA) in blocking buffer o/n, and rinsed for 1 hour in blocking buffer prior to a second round of fixation with 2% gluteraldehyde/0.1M cacodylate buffer for 30 minutes, and a final rinse in cacodylate buffer for 30 minutes. Next, the cells were rinsed in distilled water, and rinsed in 0.02 M sodium citrate for 30 minutes (to quench aldehydes). Nanogold in the samples was developed using a SilverEnhancer kit (Nanoprobes) for 5 min, and stopped using distilled water. Next, the cells were post-fixed with 0.1 % osmium-tetroxide for 30 minutes, then rinsed and left in 0.5% aqueous uranyl acetate overnight, then rinsed for 30 minutes in distilled water.

Samples were dehydrated in an ethanol series 50%, 70%, 95% and 100%, 10 minutes for each step. The cells were infiltrated with the epoxy resin Embed 812 (Electron microscopy Sciences, Hatfield, PA, USA) gel capsules inverted over the cells and hardened overnight at 60°C. Sample blocks were cut using a Leica UltraCut UC7. 60nm sections were collected on formvar/carbon coated grids and contrast stained using 2% uranyl acetate and lead citrate. Grids were viewed on a FEI Tencai Biotwin TEM at 80Kv. Images were taken using Morada CCD and iTEM (Olympus) software. Automated quantification of gold in Golgi membranes was performed with a custom script in MatLab (https://bitbucket.org/omarzaki123/golgi-gold-counter/src). The 250 nm sections for tomography were viewed using a FEI Tecnai TF20 at 200 kV with tilt angles from 60° to -60°. Data was collected using a FEI Eagle 4K X 4K digital camera. The volume reconstruction was done using IMOD and segmentation done using 3Dmod (Boulder Laboratory for 3-Dimensional Electron Microscopy of Cells, University of Colorado).

Estimation of Membrane Curvature on Tomogram Data

Membrane outlines, and where appropriate the locations of palmitate clusters, were manually annotated in EM tomograms using IMOD. These annotations, consisting of either 2D curves (in serial sections) representing Golgi membrane, or individual 3D points representing the location of palmitate clusters were loaded into python using the PyIMOD library. Local curvature was assessed at each point along the annotated membrane curves by fitting a segment of a circle to a small neighborhood (14 control points spanning ~30nm) around each point. We chose to estimate curvature from the 2D manually annotated curves rather than attempting to reconstruct a full 3D surface as the complicated Golgi morphology made linking contours between sections both time consuming and error prone. Membrane associated with palmitate was identified by performing nearest neighbor analysis between the palmitate locations and the annotated membrane. As curvature estimation was performed in 2D rather than 3D out of plane curvature is neglected and both total curvature and the palmitate curvature preference are likely to be under-estimated. Assuming a random 3D orientation, trends should nonetheless be visible.

Estimation of Proximities in STED Images

The proximity of either COPI to palmitate or COPI to a Golgi cisternal marker was assessed as follows: A threshold was chosen (20%) to identify Golgi areas labelled by palmitate and GM130. A euclidian distance transform was performed on this mask, giving the distance of every pixel in the image to the edge of the mask. Using this distance image, a cumulative histogram of COPI labelling was computed as a function of distance. This can be interpreted as the fraction of the total labelling that could be found within a given distance of the edge of palmitate or Golgi labelling. Negative distances indicate pixels which are within the Golgi mask. The code is implemented in python using the scipy toolkit and is available as part of the python-microscopy package (www.python-microscopy.org).

Purification of Recombinant Proteins from EXPI293 Cells

Plasmid encoding for FLAG-tagged TfR-mini was transfected into EXPI293 cells according to the manufacturer (Thermo Fisher), and incubated at 37°C, 8% CO_2 for 48h. Cells were pelleted at 1,000xg for 10 min, washed in PBS, and re-pelleted. Pellets from 50 ml of cell culture were resuspended in 8ml of 50 mM HEPES/KOH pH 7.3, 175 mM NaCl, 5 mM EDTA, 1mM PMSF, 1mM TCEP, protease inhibitor cocktail, and 8% (v/v) TX-100. Next, the pellets were sonicated at amplitude 30 for 1 min, and centrifuged at 800xg for 2 min before repeating the sonication. Next, the lysate was placed rotating at 4°C for 3h, then centrifuged at 20,000xg rpm for 25 min at 4°C. The supernatant was transferred to a conical tube containing FLAG-affinity resin equilibrated in lysis buffer, and rotated for 3h at 4°C. The resin was added to a column, settled, and washed with 25 ml HEPES buffer (without TX-100). AF647-NHS ester was diluted in HEPES buffer to a final concentration of 50 μM, and added to the resin, and incubated for 1 h on ice. After two additional washes, the column was washed twice with 4 ml HEPES buffer containing 50 mM OG for 10 min on ice. If indicated, thioester-bound palmitate was cleaved in 1 ml of 1.5 M neutral hydroxylamine in HEPES, and washed twice in HEPES/OG. Finally, the proteins were eluted in HEPES/OG containing 125 ng/ml FLAG peptide (Sigma-Aldrich) in 300 μl aliquots, 30 mins per elution, for a total of 1.5 ml. Elutions were analyzed on 4-20% Bis-Tris gradient gels and stained with Coomassie, or analyzed for in-gel fluorescence on a LI-COR Odyssey infrared scanner.

Identification of *S*-Palmitoylated Proteins

For acyl-PEG and acyl-biotin-exchange assays (APE, ABE) assays, cells were lysed with TEA buffer (pH 7.3, 150 mM NaCl, 50 mM TEA, 1x Protease Inhibitor Mixture (Roche)) containing 4% SDS w/v. Typically, 200 ug of total protein in 95.5 μl lysis buffer was treated with 2 μl of 0.5 M TCEP for a final 10 mM TCEP with 30 min nutation. 25 mM of N-ethylmaleimide (NEM, Sigma) was freshly made and 2.5 μl was added to the sample, followed by a 2h incubation at room temperature. The alkylation step was then terminated by a methanol-chloroform-water (MCW) precipitation, with addition of pre-chilled methanol (400 μl), chloroform (150 μl), and distilled water (300 μl). The reactions were then centrifuged at 20,000g for 5 min at 4 C. The aqueous layer was removed and 1 mL of MeOH was added before another centrifugation step at 20,000g for 3 min. Once again, the supernatant was decanted, 800 μl of MeOH were added, and the sample was centrifuged again before being dried in a speed-vacuum. The samples were resuspended in 100 μl of TEA buffer, warmed to 37 C and sonicated for 5s, before undergoing two additional rounds of MCW precipitation to ensure complete removal of NEM. The samples were then resuspended in 30 μl of TEA buffer containing 4% SDS and 4 mM EDTA, and they were treated with 90 μl of 2M neutralized NH_2OH (Sigma) dissolved in TEA buffer (pH 7.3) and containing 0.2% Triton X-100. The final concentration of NH_2OH was 1.5 M. The control samples were not treated with NH_2OH but rather TEA containing 0.2% Triton. The samples were incubated at room temperature for 1 h to overnight with nutation. Afterwards, another MCW precipitation was done, and the samples were resuspended in 30 μl TEA buffer containing 4% SDS, 4 mM EDTA. For APE assays (Percher et al., 2016), the sample was warmed to 37 C and sonicated for 5 s, before being treated with 90 μl TEA buffer containing 0.2% Triton X-100 and 1.33 mM mPEG-Mal (10 kDa). For ABE assays, HPDP-biotin was employed. The final concentration of the mPEG-Mal/HPDP-biotin was 1 mM. Samples were then incubated for 2h at room temp before a final MCW precipitation. For APE assays, the protein pellet was then resuspended in SDS-sample buffer (16% SDS), heated to 95 C for 5 min, and then loaded on a NuPAGE 4-12% Bis-Tris Gel, separated by SDS PAGE, and analyzed by Western Blot. For ABE-assays, samples were lysed in 500 μl lysis buffer (50 mM HEPES–NaOH, pH 7.4, 100 mM NaCl, 5 mM EDTA, 1% (v/v) Triton X-100, 0.5% (w/v) deoxycholate, and protease inhibitor cocktail (Roche)), and concentrated with Neutravidin-agarose (Pierce, Appleton, WI, U.S.A) prior to SDS-PAGE and Western blot.

Identification of S-palmitoylated proteins was performed employing 50 μM alkyne-palmitate for 30 min in cells overexpressing the protein of interest. The cells were then scraped and clicked to 5 μM biotin-azide (ThermoFisher, Waltham, MA, U.S.A) in a waterbath sonicator for 10 min. After 20 min additional agitation of the samples, the cells were lysed as described above, concentrated with Neutravidin-agarose and subjected to SDS-PAGE and Western blot.

Micromanipulation of Proteo-Giant Unilamellar Vesicles

Proteo-GUVs reconstitution: Giant unilamellar vesicles (GUVs) were made in a 295 mOsm sucrose solution following the classical electroformation protocol (Mathivet et al., 1996) and contained a mixture of 1,2-dioleoyl-sn-glycero-3-phosphocholine (DOPC from Avanti Polar Lipids), 1,2-dioleoyl-sn-glycero-3-phosphoethanolamine (DOPE from Avanti Polar Lipids), 1,2-distearoyl-sn-glycero-3-phosphoethanolamine-N-[biotinyl(polyethylene glycol)-2000] (ammonium salt) (DSPE-PEG-biot from Avanti Polar Lipids) and Atto 488 labeled DOPE (DOPE-Atto from Atto-Tec) at a ratio 87:10:1:0.2 mol/mol.

Prior to the experiment, 20 μl GUVs were added to 180 μl of a solution containing 15 mM Hepes/KOH pH 7.3 and glucose with a final osmolarity of 330 mOsm (HG buffer). The larger osmolarity slightly deflated the GUVs which facilitated micromanipulation and the formation of a membrane protrusion inside the micropipette. 3 μl of Alexa-647 labeled protein at 3 μM were added to this GUV solution. OG was then 50 times below it CMC, GUVs remained intact and proteins spontaneously inserted into the GUV membrane. These proteo-GUVs were used for micromanipulation.

Micromanipulation experiments: Micromanipulations were performed in a glass bottom dish (Mattek, part No. P35G-0-20-C) pre-incubated for one hour with a 10% bovine Serum Albumin Solution and extensively rinsed with HG buffer. In the dish, 10 μl of the proteo-GUVs solution and 0.1 μl of 5μm biotinylated silica beads (from Bangs Labs) were added to 400 μl of HG buffer. Because of their density, beads and proteo-GUVs settled down at the bottom of the dish where they could be seized by two micropipettes under a confocal microscope (Leica SP8). All observations were performed with a 20x air objective. When the bead was brought in contact with the proteo-GUV membrane, streptavidin-biotin bonds formed leading to a strong adhesion between the membrane

and the bead. Upon separation of the bead, a tube was pulled from the membrane as previously described (Bo and Waugh, 1989). Because the surface and volume of the proteo-GUV remained constant during the experiment (Hochmuth et al., 1982), the radius of the tube, r_t, was obtained from the displacement of the protrusion in the pipette, ΔL_p, upon displacement of the bead, ΔL_b, through the relation: $r_t=(1-r_p/R_v)r_p DL_v/DL_t$, where r_p is the micropipette radius and R_v the vesicle radius.

Relative concentration of the protein in the membranes: The fluorescence intensities of the protein and DOPE-Atto were measured in both membranes: $I_{GUV/prot}$, $I_{GUV/Lip}$ in the proteo-GUV respectively and $I_{tube/prot}$ and $I_{tube/Lip}$ in the tube respectively. The relative density of the protein in the tubes and in the proteo-GUV, R, was then obtained, as previously proposed (Sorre et al., 2009), by: $R= [I_{tube/prot}/I_{GUV/prot}]/[I_{tube/Lip}/I_{GUV/Lip}]$.

QUANTIFICATION AND STATISTICAL ANALYSIS

Statistical analysis was performed using GraphPad Prism 6 (GraphPad Software, La Jolla, CA, USA) for unpaired, two-tailed t-tests. Differences were considered significant if P-value <0.05(*), <0.01(**), or <0.001(***). Automated quantification of gold particles in Golgi membranes was performed with a custom script in MatLab (MathWorks, Natick, MA, USA): https://bitbucket.org/omarzaki123/golgi-gold-counter/src. Pearson's correlation coefficient was calculated using the ''co-localization threshold'' plugin in ImageJ (confocal sections), or Volocity software (Z-stacks; Quorum Technologies, Lewes, UK).